Biomembrane Investigations with Molecular Rotors

by

Matthew E. Nipper

(Under the direction of Mark A. Haidekker)

Abstract

Molecular Rotors are unique fluorescent reporters that exhibit photoinduced intramolecular rotation. The amount of molecular rotation is a function of the local free volume. This relationship results in a quantum yield that is proportional to the solvent viscosity. Molecular rotors are an ideal candidate for characterizing membrane viscosity because of their excellent temporal and spatial response. Membrane viscosity has shown high correlation with the physiological state of the cell. The magnitude of these changes are minuscule and often below the limit of detection for mechanical methods. Molecular rotors are ideally suited for this application. We have synthesized and characterized molecular rotors for the purpose of membrane viscosity characterization. The primary objective of this research is to progress these efforts by implementing a ratiometric family of molecular rotors. To optimize these efforts, we have constructed a custom spectrophotometer for the purpose of correcting non-ideal optical properties. Furthermore, we have simulated conventional membrane characterization techniques for the purpose of comparison and experiment optimization. Quantification of membrane viscosity may provide a useful tool for researchers and clinicians alike.

Index words: Molecular Rotors, FRAP, Liposomes, Viscosity, Membrane

BIOMEMBRANE INVESTIGATIONS WITH MOLECULAR ROTORS

by

MATTHEW E. NIPPER

B.S., The University of Missouri, 2006
M.S., The University of Missouri, 2007

A Dissertation Submitted to the Graduate Faculty
of The University of Georgia in Partial Fulfillment
of the
Requirements for the Degree

DOCTOR OF PHILOSOPHY

ATHENS, GEORGIA

2010

Biomembrane Investigations with Molecular Rotors

by

Matthew E. Nipper

Approved:	
Major Professor:	Mark A. Haidekker
Committee:	William S. Kisaalita Caner Kazanci

Electronic Version Approved:

Maureen Grasso
Dean of the Graduate School
The University of Georgia
August 2010

TABLE OF CONTENTS

Page

CHAPTER

List of Figures

List of Tables

CHAPTER 1

FLUORESCENCE

1.1 OVERVIEW

Luminescence is the emission of a photon from an electronically excited molecule. Upon reaching the excited state via an incident excitation energy, the molecule can enter a number of pathways. An overview of this process is illustrated in Figure 1.1 [3]. Figure 1.1 depicts the singlet state energy levels of S_0, S_1, and S_2 respectively. The smaller lines at each energy state represent vibrational states. Upon reaching S_1 or S_2 the electron can follow a number of pathways. The return from S_1 back to S_0 is energetically most favorable. This is due to the fact that the electrons in S_0 and S_1 have opposite paired spins. This enables a rapid return to the ground state which is otherwise termed a radiative event. This radiative event is referred to as fluorescence emission and occurs on the $10^{-9}s$ time scale. It is possible for the electron to return to the ground state without photon emission. This is described as a non-radiative event [3].

Phosphorescence also results in photon emission but is a much more rare event compared to fluorescence. Phosphorescence is a result of intersystem conversion from the S_1 to T_1 state and the subsequent photon release upon returning to the ground state. The frequency of this particular event is low given the same spin paired electrons are not energetically favorable. Internal relaxation occurs when electrons move down internal vibrational levels for the lowest possible configuration as seen in Figure 1.1. In both fluorescence and phosphorescence, photon emission occurs only when the electron returns to the S_0 ground state.

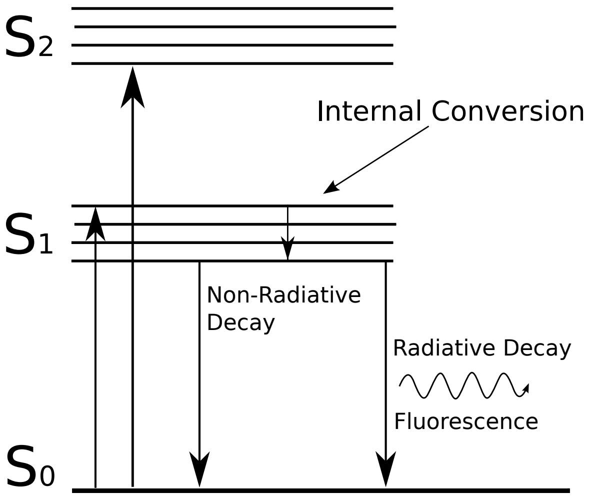

Figure 1.1: Jablonski diagram and relative positions of absorption, fluorescence, and phosphorescence spectra. Vertical lines describe transitions between state. S_0-singlet ground state, S_1, S_2- first and second excited states

In the case of photon emission, and in particular, fluorescence, the wavelength of the emitted light is longer than that of the absorbed excitation light. This is always the case for a given fluorophore because of the energy loss in the vibrational modes. The shift is independent of the excitation wavelength and unique for a given fluorophore. The distance between the absorption and emission spectra peaks is defined as the Stokes's shift. Examining the equation $E = \frac{h}{\lambda}$, it becomes clear that a longer wavelength is the result of an energy loss.

The ratio of the radiative events to total photon absorption is termed the quantum yield. Equation 1.1 describes this relationship where k_r and k_{nr} are the radiative and non-radiative events respectively. The quantum yield of a fluorophore is ≈ 1 when $k_{nr} << k_r$, as is the particular case with the fluorophore rhodamine. The quantum yield of a fluorophore can never equal exactly 1 due to the abundant non-radiative pathways present.

$$\phi = \frac{k_r}{k_r + k_{nr}} \tag{1.1}$$

The quantum yield relationship is directly related to the lifetime of the fluorophore. Fluorescence lifetime is the amount of time the fluorophore remains in the excited state before the photon is released. Typically, fluorescence lifetimes are on the order of $10^{-9}s$. The fluorescence lifetime is calculated using Equation 1.2.

$$\tau = \frac{1}{k_{nr} + k_r} \tag{1.2}$$

Fluorescence decay is an isotropic random process and correspondingly equation 1.2 describes the average lifetime for a population of fluorophores. For molecules with one lifetime, a single exponential decay is used to describe the function over time. At $t = \tau$, 63% of the fluorophores have undergone fluorescence emission and returned to the ground state while the remaining 37% decay at $t > \tau$. The intrinsic lifetime of a fluorophore is the lifetime in the absence of non-radiative processes and is defined is Equation 1.3.

$$\tau_n = 1/k_r \tag{1.3}$$

The intrinsic lifetime can also be found by combining Equations 1.1-1.3. Alternatively, by combining the absorption and emission spectra with the molar extinction coefficient, the intrinsic lifetime can be calculated. Often the two calculations do not yield the same results. A number of confounding factors contribute to the calculation of the intrinsic lifetime. Among these are solvent specific effects, refractive index changes, and changes in excited states geometry. These effects make lifetime measurement difficult, and in turn, require the use of high resolution spectrometers cable of high frequency data collection.

1.2 Detection and Instrumentation

Fluorescent molecules have both molecule-specific emission and excitation spectra. The excitation spectra is the complete range of wavelength response in which photon absorption occurs. Correspondingly, the emission spectrum is the wavelength range in which fluorescence emission occurs. The emission spectrum peak always has a longer wavelength for a corresponding excitation spectrum peak. Spectra are most commonly is reported as intensity over wavelength (denoted by λ) but may also be represented by frequency, ν, or wavenumber, ν, which has units of cm^{-1}. In an ideal system, the excitation and emission spectra could be superimposed upon each other. Often, this is not the case due to wavelength specific responses in the instrumentation along with confounding signals that arise from the background. Understanding the instrumentation is key for background correction. All spectrometers are comprised of an excitation source and and emission measurement instrumentation. A common instrument design is shown in Figure 1.2.

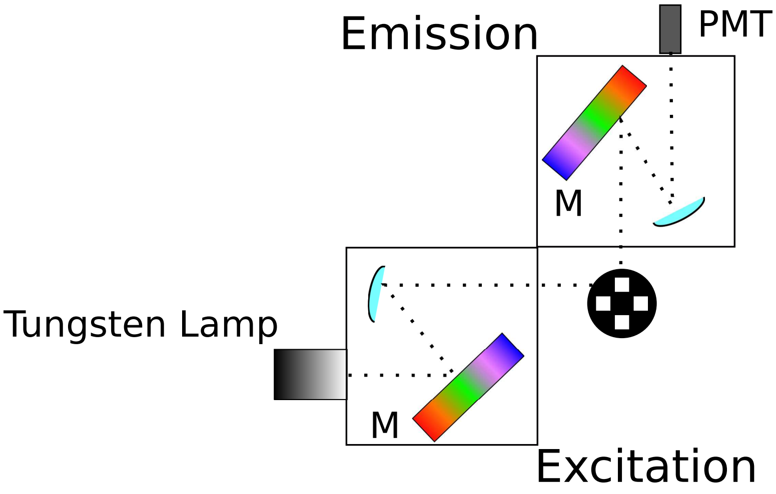

Figure 1.2: A common spectrophotometer design. The excitation unit is composed of a tungsten lamp and a motor controlled monochromator (M) for wavelength specification. The emission unit is equipped with a separate monochromator and a photomultiplier tube (PMT)

1.2.1 Light Sources

Most commercial spectrometers are equipped with tungsten arc discharge lamps with an excitation monochromator. The purpose of the monochromator is to provide a means to select a specific excitation wavelength. The advantages of the lamp is that it has a wide distribution of wavelengths. This allows for deep UV as well as Near Infrared excitation. One disadvantage is the wavelength dependent emission of the lamp and the proclivity of noise that arise from current spikes in the power source. The excitation signal is often measured and divided from the resulting emission scan to counteract these effects. The uneven lifetime of the bulbs along with the high sensitivity to heat are effects that must be accounted for and corrected.

Light Emitting Diodes (LEDs) are becoming increasingly more common in spectrometers. LEDs are desirable because of their extremely long lifetime and easily constructed current controlled driver circuits. LED excitation units do have a unique set of construction considerations. The spectral output is approximately a Gaussian distribution with a full width half maximum (FWHM) of typically 20 nm around the center wavelength and can be narrowed using bandpass optical filters or a monochromator. LEDs also have a broad viewing angle which needs to be collimated with free space lenses. While the intensity of a modern high-power LED unit is quite high ($\approx$ 100 lumens), a large amount of light is lost during collimation. This is due to the wide viewing angle.

Laser diode modules are easily employed in the spectrometer design. Lasers are highly desirable because of the constant spectrally and spatially coherent output. The light output is focused and polarized making polarization experiments easy to perform. Lasers are the ideal point excitation source because of the pre-collimated light source and constant intensity output. A major consideration for laser excitation units is the cost prohibitive selection at specific wavelengths and the necessity for multiple lasers if a wide excitation spectrum is desired. A laser does not however need any additional filters.

1.2.2 Filtering of Light

Filtering is a key component of any spectrometer. Filters are often employed in both the excitation and emission signal conditioning. Shortpass, longpass, and bandpass filters allow for the separation of signals. Dichroic mirrors are commonly used to separate and redirect emission from the original excitation beam. The common denominator in most commercial spectrometers is the monochromator. Monochromators are curved mirrors with a special grating that results in a light beam to be separated according to wavelength. Additional slits allow for the selection of a particular wavelength. A monochromator can provide very accurate wavelength separation when controlled via motor. Often the monochromator is curved to act as a collimating mirror for beam focusing to the detection device. Depending on the sensitivity of the device, signal attenuation may need to be introduced. Neutral density filters allow for signal attenuation if desired and are used if emission/excitation intensities are near the upper threshold of detector sensitivity. Detector sensitivity is a major concern for all methods and in particular photomultiplier tubes (PMTs).

1.2.3 Detection & Quantification

PMTs are the detector of choice in spectrometers. They provide an optimal balance of sensitivity across a wide range of wavelengths. PMTs exhibit an ideal linear current that is proportional to incident light and can be made sensitive enough to register individual incident photons. The main sensing mechanism is the photocathode and dynode cascade pairing. The photocathode is held at a high negative voltage. The primary dynode is also held at a high negative voltage that moves towards zero further down the cascade. Upon incident photon striking, $5 - 20$ electrons are released and accelerated towards the primary dynode [3]. The amount of electrons released is a function of the base voltage applied. This voltage must be constant and in order to preserve the linear response of the electron cascade. This wave of electrons then cascades down the dynode chain upon reaching the terminal anode being multiplied at each dynode. The resulting signal is an amplified average of the initial photons striking the photocathode. The output is linear in respect to photon changes up to high intensities. The PMT may exhibit non-linear response at high photon intensities. In some cases, the emission intensity may be high enough to use a photodiode. More often, a special photodiode can be used, namely an avalanche photodiode. These photodiodes provide an excellent balance in both cost and sensitivity

Understanding the photophysical phenomenon responsible for fluorescence emission is essential for the interpretation of spectroscopic experiments. Fluorophores may exhibit a range of property changes dependent on the solvent. Examples of solvent dependent photophysical processes are quenching and solvochromatic shift. The response to the physical environment may result in changes in the quantum yield or resonance energy transfer efficiency. Molecular rotors are a class of fluorophores that exhibit a solution dependent quantum yield. This family of fluorophores will be described in the following chapter. Identifying and understanding solvent effects are necessary to extract the maximum information for an experiment. Equally important, is understanding the instrumentation and the artifacts it may produce in a fluorophore experiment. Hardware optimization is key for measuring the spectroscopic properties of molecular rotors.

Chapter 2

Molecular Rotors

2.1 Introduction

Molecular rotors are a group of fluorescent molecules that form an intramolecular charge transfer mechanism which exhibits a twisting motion in the excited state. These fluorophores are alternatively referred to as twisted intramolecular charge transfer (TICT) complexes. TICT complexes can return to ground state from either the local excited (LE) or from the twisted state. The energy differences between the LE and twisted states to the ground state are different and determine the fluorescence emission, or lack thereof, from a TICT complex. The central twisting action of these molecules ultimately reveal information about the physical properties of the surrounding medium. In particular, the relaxation rate from the twisting state is directly influenced by the solvents polarity and microviscosity. This has led to the employment of molecular rotors as mechanofluorescent reporters [1].

The TICT mechanism was first observed in the molecule p-N,N-dimethylaminiobenzonitirile (DMABN) which can be seen in Figure 2.1. Lippert [4] reported the dual emission of DMABN in polar solvents. The red-shifted emission was found to be higher compared to the primary emission while the overall intensity was declining. Interestingly, the overall emission intensity is increased in high viscosity solvents. Advances in this field have led to the synthesis and study of fluorophores that exhibit the formation of an intermolecular charge transfer (ICT) state. The formation of this state results in a highly polar sensitive molecule in the excited state.

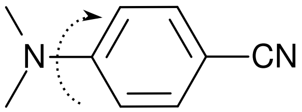

Figure 2.1: Chemical structure of the molecule p-N,N-dimethylaminiobenzonitirile (DMABN). The dotted arrow indicates the bond of rotation resulting in the TICT state formation.

Rotkiewicz *et al.* [5] formulated the TICT theory whereby a molecule can exhibit intermolecular twisting around a single bond as seen in the case of DMABN in Figure 2.1. Deexcitation can occur from either a planar locally excited (LE) or from the twisted state resulting in different deexcitation energies. The anomalous red-shifted emission previously described in DMABN can be explained as a deexcitation from the lower-energy twisted state. This effect is amplified in other classes of molecules which may result in deexcitation without photon emission. Fluorescence emission and twisted state formation are competing processes in the LE state where TICT state formation is much faster.

Formation of the twisted state is highly dependent on the physical properties of the surrounding media. Both steric hindrance and solvent polarity affect the dynamics of twisted state formation. Steric hindrance acts to reduce twisted state formation while highly polar solvents may provoke dipole reorientation with the addition of hydrogen bonds on the fluorophore thus enhancing TICT formation. The dynamic nature of TICT molecules have been used to study the kinetics of competitively and consecutively coupled configurations [6]. Static processes such as quenching and photochemical effects have also been probed with TICT fluorophores [6]. The advantages in using TICT molecules to act as mechanofluorescent reporters arise from the high sensitivity to changes in solvent physics. The end product, changes in fluorescent properties. begin at the molecule's ability to exhibit dynamic photophysical properties.

2.2 PHOTOPHYSCIAL PROPERTIES

Electron energy transfers between the lowest unoccupied molecular orbital (LUMO) and the highest occupied molecular orbital (HOMO) are the relevant states that are considered when evaluating the effects on twisted state physics. The LUMO-HOMO transition typically promotes an electron to an anti-bonding state $*$. Typically fluorescence involves π and σ orbital transitions and most commonly arises from a $\pi \rightarrow \pi^*$ transition. Also possible, are transitions of non-bonding n electrons to the anti-bonding π^* and σ^* states. All intermolecular charge transfer molecules are comprised of a donor/acceptor group and connected via a π-conjugation system. The donor provides n-electrons that are transferred to the unoccupied orbitals of the acceptor. The π-conjugation between the donor and acceptor results in negligible spatial overlap of the orbitals of the donor and acceptor subgroups.

Upon promotion to a higher molecular orbital, electrons often relax to a number of vibrational states before returning to the ground state and photon release. This relaxation is a form of energy loss and, as described earlier, leads to a spectral shift known as Stokes's Shift. Analogously, the TICT state formation can be considered a type of vibrational state that results in energy loss. The twisting of the molecule is the result of an unbalanced dipole moment which leads to a configuration change of the donor nitrogen from a pyramidal to a planar charge transfer state. Figure 2.2 [7, 4, 8] illustrates the energy differences in a TICT configuration. It becomes apparent that the natural tendency is to return to the planar state. To reach the TICT excitation state, a minimum energy level must be overcome in the LE state. Research has found that mechanisms that delay the planar formation, such as placing an amino group within a heterocyclic ring [9], increase the energy barrier between the LE and TICT states. Solution effects such as solvent polarity, decrease this energy barrier whereas, viscosity increases this barrier for TICT state formation in DMABN [8].

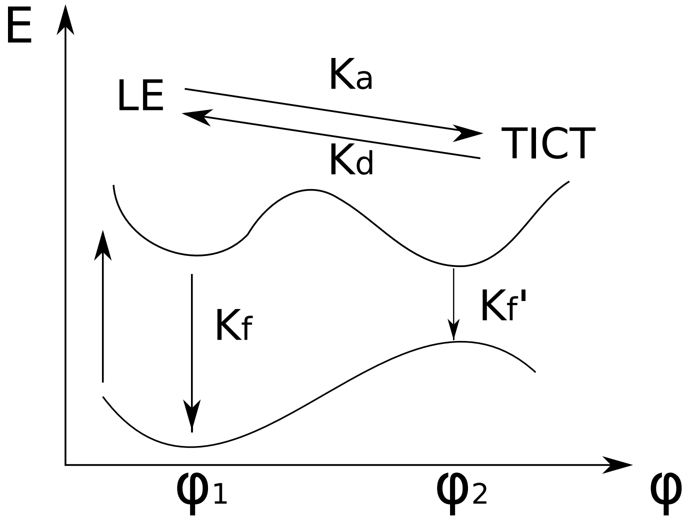

Figure 2.2: Illustration of the ground state and excited state energies as function of rotational angle, φ, for a TICT molecule. Upon photon absorption, the molecule can either return to the ground state with a rate k_f or exhibit intramolecular rotation with a rate k_a. As the rotation angle φ increases, the molecule can either return to the ground state with a rate of k'_f or return to the LE state with a rate of k_d. In the twisted state configuration, $k'_f \gg k_d$, so the predominant pathway is a return to ground state. Adapted from Haidekker *et al.* [1]

Intermolecular rotation as a means to return to the ground state leads to a loss of energy. This energy loss is responsible for the solvatochromic shift in emission commonly observed in aminobenzonitriles. The ratio of the quantum yields of the TICT and LE states can be found using the forward and backward reaction rates respectively. The ratio of the quantum yields of the TICT state, Φ_{TICT}, and the locally excited state Φ_{LE} is found using Equation 2.1 [10], where τ_{CT} is the TICT lifetime, k'_f is the deexcitation rate from the twisted state, k_f is the deexcitation rate from the LE state, k_a is the rate of TICT formation from the LE state, and k_d is the reverse rate. In other words k_d is the return to the LE state from the TICT state. Generally $k_a >> k_d$ making the TICT state relaxation dominant. Thus, molecular rotors that exhibit high radiation-less deexcitation have a lower quantum yield.

$$\frac{\Phi_{TICT}}{\Phi_{LE}} = \frac{k'_f}{k_f} \cdot \frac{k_a}{k_d + 1/\tau'_{CT}} \tag{2.1}$$

TICT state formation and the subsequent quantum yield is dependent on the ability of the molecule to twist in the local environment. A confounding effect is that of solvent polarity. Solvent polarity works in opposite effect to that of solvent viscosity. The effects of solvent polarity on emission spectra in DMABN are well documented [11]. TICT molecules exhibit photoinduced charge separation which results in an increased dipole moment. Polar solvent molecules orient around this charge separation and as a result the entropy of the system is decreased. Relaxation results in the return of polar molecules to a more random orientation and the entropy is increased. A consequence of this behavior is an observed increased relaxation rate that produces a bathochromic shift in emission spectra. The dielectric constant ϵ, determines the magnitude of this effect. This relationship is defined by the Lippert-Mataga equation seen in Equation 2.2,

$$\bar{V_a} - \bar{V_f} = \frac{2}{hc} \cdot \left(\frac{\epsilon - 1}{2\epsilon - 1} - \frac{n^2 - 1}{2n^2 + 1} \right) \cdot \frac{\mu_e - \mu_0}{a^3} \tag{2.2}$$

where, $\bar{V_a}$ is the absorption wavenumber, $\bar{V_f}$ is the wavenumber of peak fluorescent emission, h is Planck's constant, c is the speed of light, n is the refractive index, and μ_c and μ_0 are the excited and ground state dipole moments of the fluorophore, respectively. Finally, a is the radius of the void volume in which the fluorophore is located. The polar environment of a solvent directly affects some TICT molecule's quantum yield. The polar sensitivity observed in TICT fluorophores is closely related to the ability of the fluorophore to form hydrogen bonds in the surrounding solvent. Hydrogen bonding results in spectral shifts and may cause changes in ordering of states. The changes in state ordering have been reported in carbonyl and heterocycle compounds which results in a lowering of the energy barrier between the lowest ($n \rightarrow \pi^*$) and ($\pi \rightarrow \pi^*$) singlet states [12, 13, 14]. Hydrogen bonding acts in a similar fashion to polar-polar interactions on TICT molecules. Similar to polar-polar interactions the non-radiative relaxation rates are increased, however, the magnitude of this effect is much smaller in magnitude.

Molecular rotors exhibit a number of sensitivities to the local solvent that result in changes in spectral data. Molecular rotors report change in the local solvent through spectral shifts, and changes in quantum yield and fluorescence lifetime. The ability to measure a solvent's viscosity has become a popular application for these fluorophores. While viscosity is a bulk solution property, the micro-environment is altered and TICT molecules are uniquely positioned to quantify these characteristics.

2.3 Application - Viscosensitive Reporters

The use of molecular rotors as fluorescent viscosity sensors has evolved from the sensitivity to changes in the local physical properties. The ability to measure changes in a bulk property is proportional to changes in the free volume. This relationship has been established between the diffusivity D of fluorophore, and the bulk viscosity η of a solution, as defined in the Stokes-Einstein equation. It should be noted that the proportionality between diffusivity and bulk viscosity is always an approximation. There are solvent-specific anomalies such as electrostatic interactions, hydrogen bonding, and anisotropic conditions that prevent measurement of a direct proportional relationship. Foïster and Hoffman were pioneers in their experiments with triphenylamine dyes to establish this relationship [15]. The chemical structure of triphenylamine can be seen in Figure 2.3

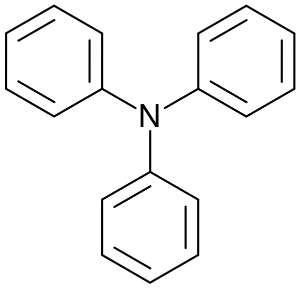

Figure 2.3: Chemical structure of triphenylamine.

The Förster-Hoffman equation begins with relating the microfriction $\varkappa$ in the Debye-Stokes-Einstein (DSE)equation. The following derivation is adapted from Haidekker *et al.* [16]. The DSE equation is defined in Equation 2.3

$$\varkappa = 8\pi r^3 \eta \tag{2.3}$$

where η is the bulk viscosity of the solvent and r is the effective radius of one phenyl group of the triphenylamine dye. The three arms of the dye are considered rotational masses and obey the differential equation of rotation as defined in Equation 2.4,

$$\theta \frac{d^2\varphi}{dt^2} + \varkappa \frac{d\varphi}{dt} + \alpha(\varphi - \varphi_0) = 0 \tag{2.4}$$

where φ is the angular deviation from the equilibrium state φ_0, α is the spring constant of an imaginary torsional spring that models the ground-state energy difference between the twisted and planar state, θ is the rotational inertia of the phenyl group, and $\varkappa$ is the microfriction of coefficient. The microfriction dampens the rotation and when $\varkappa >> 4\varkappa\theta$, the phenyl group returns from its deflection angle φ to the planar state φ_0 with exponential decay dynamics described by Equation 2.5,

$$\varphi(t) = \delta \exp\left(-\frac{t}{T^*}\right) + \varphi_0 \tag{2.5}$$

where δ is the difference between the two rotation angles where the minimum S_1 energy and the minimum S_0 energy exist, and T^* is the characteristic relaxation time constant with $T^* = \varkappa/\alpha$. This establishes the relationship between relaxation time and the solvent microviscosity and electrostatic forces. Foïster and Hoffman relate the quantum yield to the relaxation time with with a function $B(\varphi)$ that describes the rate of the deactivation process through conformational changes, $B(\varphi) = \beta(\varphi - \varphi_0)^2$ where β is a proportionality constant. Through this definition the probability $\varrho(t)$ of a molecule being in the excited state is defined as

$$-\frac{d\varrho}{dt} = \left(\frac{1}{\tau_s} + B(\varphi)\right)\varrho(t) \tag{2.6}$$

where τ_s is the lifetime of the dye in the absence of rotational deexcitation. The typical rate given by Forster and Hoffmann is $\tau_s = 1\,ns$. The quantum yield ϕ_F of the dye is defined in Equation 2.7.

$$\phi_F = \frac{1}{\tau_0}\int_0^\infty \varrho(t)dt \tag{2.7}$$

In Equation 2.7, τ_0 is not explicitly listed but assumed to be the intrinsic lifetime in the absence of factors that would increase k_{nr}. A typical value listed is in the range of $2\,ns$. Combining Equations 2.5 and 2.6 yield Equation 2.8.

$$-\frac{d\varrho(t)}{dt} = \left[\frac{1}{\tau_s} + \beta\cdot\delta\cdot\left(1-\exp\left(-\frac{t}{T^*}\right)\right)^2\right]\varrho(t) \tag{2.8}$$

Equation 2.8 is simplified by examining the extreme cases, i.e., when viscosity is at the minimum and maximum. In the first scenario, where solvent viscosity is very low, the quantum yield dependency on solvent properties is minimized and is defined as

$$\phi_F \approx \frac{1}{\beta\cdot\tau_0\cdot\delta^2}. \tag{2.9}$$

Conversely, when solvent viscosity is very high, non-radiative decay is minimized and the quantum yield is found in Equation 2.10,

$$\phi_F \approx \frac{\tau_s}{\tau_0}\left(1-\frac{6\sigma^2}{\eta^2}\right) \tag{2.10}$$

where σ is a dye-dependent constant that contains all viscosity-independent variables $(\alpha, \beta, \delta, r, \text{and}\, \tau_s)$ as defined in Equation 2.11.

$$\sigma = \left(\frac{\alpha^2\beta\,\delta^2\tau_s^3}{192\,\pi^2 r^6}\right)^{1/2} \tag{2.11}$$

The constant σ has units of viscosity. Assuming $r \approx 2x10^{-10}m$ and the energy resulting from the potential differences $\alpha \approx 10^{-9}J$, a typical value is $\sigma = 100\cdot$ Pa s. For the limiting case of $\eta \gg \sigma$, the maximum achievable quantum yield found via Equation 2.10 becomes $\phi_F \approx \tau_s/\tau_0$. For intermediate viscosities when $\eta \ll \sigma$, Equation 2.7 is simplified and becomes Equation 2.12.

$$\phi_F \approx 0.893 \cdot \frac{\tau_s}{\tau_0} \left(\frac{\eta}{\sigma}\right)^{2/3} \tag{2.12}$$

All dye dependent constants can be combined into one final constant C, and Equation 2.12 then becomes the simplified form Equation 2.13

$$\phi_F = C \cdot \eta^x \tag{2.13}$$

which is commonly known as the Förster-Hoffmann equation. In Equation 2.13, all variables are considered to be unitless. Interestingly, the value of $x = 2/3$ is a fixed value as the consequence of an integration step. Experimental results have yielded lower values of x.

The viscosity dependent rotation has been described with a different mechanism that relates the solvent effects with the molecular rotor emission. Loutfy *et al.* assumed a proportionality of the diffusion constant D of the rotor with the rotational reorientation rate k_{OR}. The Debye-Stokes-Einstein (DSE) model defines D as

$$D = \frac{1}{6Vsg} \cdot \frac{kT}{\eta} \tag{2.14}$$

where T is the absolute temperature, k is Boltzmann's constant, η is the viscosity of the solvent, V is the fluorescent dye volume, s is the boundary condition, and g is the shape factor. If rotational diffusion outweighs the reorientation rate, Equation 2.15 is true:

$$k_{or} \propto D \propto \frac{kT}{\eta} \tag{2.15}$$

Equation 2.15 has been validated by several studies [17, 18], but deviations have been reported and attributed to saturation effects. The temperature dependent emission of several molecular rotors in multiple studies was studied and found to exhibit systematic deviation form the DSE model [19]. The reorientation rate was found to behave analogous to the Gierer-Wirtz model[20] described in Equation 2.16,

$$k_{or}\frac{\eta}{T} = a + b\left(\frac{\eta}{T}\right)^{1-x} \tag{2.16}$$

where a and b are constants. Contrary to the DSE model, the Gierer-Wirtz model considers the solvent and solute as finitely shaped spears. Vogel and Rettig adapted this model to produce Equation 2.16 [21], which reduces to the DSE model for k_{OR}, Equation 2.15, when $x = 1$. Molecular volume is best described as the void space surrounding a spherical representation of a molecule. Doolittle continued this idea and related free volume and viscosity empirically in Equation 2.17 [22],

$$\eta = A \cdot exp\left(B\frac{V_o}{V_f}\right) \tag{2.17}$$

where A and B are experimental constants, V_o is the van der Waals volume of fluorescent dye, and V_f is the fluid free volume. Loutfy and Arnold [19] demonstrated experimentally that the non-radiative decay rate k_{nr} is a function of the free volume and described by Equation 2.18 [23]

$$k_{nr} = k_{nr}^{\circ}\exp(-x'\frac{V_0}{V_f}) \tag{2.18}$$

where k_{nr} is an intrinsic solvent-independent relaxation rate and x' is a solvent-dependent constant. Substituting the exponential term in Equation 2.17 into Equation 2.18 replaces the free-volume term with the bulk solvent viscosity and yields Equation 2.19 which describes a viscosity-dependent non-radiative decay.

$$k_{nr} = k_{nr}^{\circ}\left(\frac{\eta}{A}\right)^{-x} \tag{2.19}$$

In Equation 2.19, x now encompasses Doolittle's constant B so $x = x'/B$. The fluorescent quantum yield is defined as the ratio of the radiative relaxation rate k_r to both the radiative and non-radiative rates. This relationship is described by Equation 2.20

$$\phi_F = \frac{k_r}{k_{nr} + k_r} \approx \frac{k_r}{k_{nr}} \tag{2.20}$$

For the case of $k_{nr} \gg k_r$, the approximation of k_r/k_{nr} is valid. Substitution of Equation 2.19 into Equation 2.20 results in Equation 2.21

$$\phi_F = \frac{k_r}{k_{nr}^{\circ}} \cdot \left(\frac{\eta}{A}\right)^x \tag{2.21}$$

where the solvent-independent constants k_r, k_{nr}, and A^x can be combined into a constant C, which is essentially Equation 2.13. In direct contrast to the Foȑster-Hoffman derivation, Loutfy *et al.* claim x is not a rigid value set at 2/3, but instead dependent on both the dye and solvent. The solvent-dependent parameter A in Equation 2.17 establishes the need for calibration for every dye-solvent pairing before molecular rotors can be used to measure solvent viscosity.

The research starting by Förster and Hoffmann and continued by Loutfy *et al.* firmly establishes the power-law relationship between solvent viscosity and the quantum yield of molecular rotors. The ability to characterize viscosity via fluorescence reporter has been of great interest in a number of fields with multiple applications. Molecular rotors provide excellent temporal and spatial resolution for viscosity measurements compared to traditional fluorescent techniques. One emerging field has been the use of molecular rotors to characterize membrane viscosity within the phospholipid bilayer.

CHAPTER 3

CHARACTERIZING MEMBRANE VISCOSITY VIA FLUORESCENT REPORTERS

The formal definition of viscosity is defined as an isotropic fluid's resistance to flow. Viscosity governs the strain rate generated by an applied shear stress [24]. The notion of viscosity has been adapted by membrane biologists to qualitatively characterize the phospholipid bilayer. Membrane biologists have adapted this definition to characterize the fluidity, or ease of movement, within a membrane. Characterizing the membrane is of great interest due to the many roles it plays in physiological processes. Membrane physics directly influence the behavior of membrane-bound proteins [25, 26]. Changes in membrane viscosity have also been linked with the onset of disease states. Particular examples include atherosclerosis [27], cell malignancy [25], hypercholesterolemia [28], and diabetes [28, 29]. Red blood cells and platelet membranes have been observed to have higher membrane viscosity in patients with diabetes. This behavior is believed to contribute to the inability of membrane-bound insulin receptors to undergo aggregation [29, 30]. Conversely, decreased membrane viscosity has been reported in leukocytes of patients with Alzheimer's disease. The decrease in viscosity is believed to facilitate aggregation of the Amyloid Precursor Protein, a fragment of which is deposited in the brain as insoluble plaque [31]. Patients with liver disorders, including alcohol-induced diseases, showed higher erythrocyte membrane viscosity, which correlates highly with liver dysfunction [32]. In addition, increased membrane viscosity has been linked with the aging process. The research that studies the correlation between membrane physics and physiological condition is extensive and well documented.

The initial attempts at characterizing membrane viscosity were originated in mechanical methods. Recent studies have been conducted on Mesenchymal Stem Cells using partial membrane aspiration with a micro pipette [33]. In this protocol, a stem cell is partially aspirated and allowed to equilibrate to a pressure P. The pressure is then increased at discrete steps ΔP. The aspirated cell length, L, is measured under microscopy with a CCD camera. Equation 3.1 relates the length of the aspirated portion of the cell, L as a time dependent function,

$$L(t) = \frac{\Phi a \delta P}{\pi k_1}\left[1 - \frac{k_2}{k_1 + k_2} e^{\frac{-t}{\tau}}\right] \tag{3.1}$$

where k_1 and k_2 are elastic parameters, a is the inner pipette radius, and τ is a time constant. Φ is a dimensionless parameter, with a value of 2.0, that accounts for the wall thickness of the pipette. This technique assumes a boundary condition of zero axial displacement at the micro pipette end. The membrane viscosity, μ, is a function of the elastic parameters k_1, k_2, and the time constant τ, as seen in Equation 3.2.

$$\mu = \frac{\tau_1 k_1 k_2}{k_1 + k_2} \tag{3.2}$$

The membrane viscosity can then be calculated by using non-linear regression and solving for μ. This technique provides bulk information on the particular section of membrane aspirated. The deflection of the membrane also may impact the physiological function of membrane proteins possibly skewing the results.

Magnetic rheometry is another documented method for measuring membrane viscosity. In this protocol, magnetic beads are attached to integrin receptors in fibroblasts [34]. Non-magnetic latex beads are also attached to act as a control. The fibroblasts is then exposed to a uniform magnetic field. When the magnetic force is applied, the beads exhibit a three-phase creep response consisting of an elastic deformation, a stress relaxation, and a viscous flow. By measuring these parameters as a function of time, the membrane viscosity can be calculated. The magnetic rheometry experiments yielded a calculated viscosity nearly one order of magnitude less than that of the micropipette aspiration experiments [34]. The use of magnetic particles requires cost-prohibitive equipment that requires long experiment times.

Additionally, the particles may interact with the cellular surrounding providing measurement artifacts and ultimately altering the cellular conditions.

Mechanical based techniques are unable to provide the high spatial and temporal resolution required for cellular studies. Most importantly, mechanical methods are unable to relay information on the inner hydrophobic core of the membrane where discrete regions of viscosity difference may exist. Fluorescent methods lend themselves as an attractive option for studying cellular physics. Fluorescence based methods provide the discrete time and space response needed for studying cellular dynamics. Of the multiple fluorescent methods, fluorescence anisotropy and fluorescence recovery after photobleaching (FRAP) are the most common.

3.1 Fluorescence Anistotropy

The quantification of anisotropic fluorescence is one method for revealing the physical properties of a particular solvent. In a typical anisotropy experiment a population of randomly oriented fluorophores is excited with a polarized light source. Upon excitation, the fluorophores with their absorption moments along the axis of polarization are preferentially excited. The distribution of excited fluorophores is no longer random. Upon depolarization, the fluorophores return to a uniform random distribution. As the depolarization is occurring the fluorescence emission is also polarized. A schematic of a typical anisotropy experiment is shown in Figure 3.1.

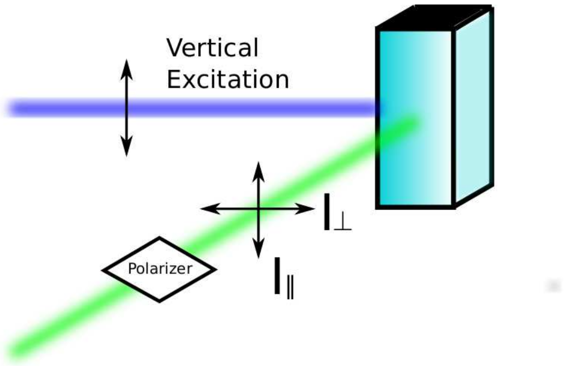

Figure 3.1: Schematic of a typical fluorescence anisotropy experiment. A polarized light source is used for excitation. A polarizer is placed in front of the detector to quantify the anisotropy.

The speed at which depolarization occurs is a function of the rotational diffusion. Rotational diffusion is a function of both the solvent viscosity and the size profile of a particular fluorophore. This process occurs on a timescale faster than that of fluorescence emission. For fluorophores in high viscosity solvents the rotational diffusion is impeded and the polarized fluorescence is measured against the excitation and the anisotropy (r) is calculated in Equation 3.3.

$$r = \frac{I_\parallel - I_\perp}{I_\perp + 2I_\parallel} \tag{3.3}$$

By dividing by difference by the total sample intensity, $I_T = I_\parallel + 2I_\perp$, the anisotropy becomes a unit-less measurement. Anisotropy experiments provide information on a population of fluorophores in manner similar to fluorescence lifetime measurements. For a population of fluorophores, the anisotropy can be defined as

$$\bar{r} = \sum_i f_i r_i \tag{3.4}$$

where f_i is the fractional fluorescence, and r_i is the individual anisotropy. The decay of a population of fluorophores of a pulsed excitation beam is described in Equation 3.5

$$r(t) = r_0 e^{-t/\theta} \tag{3.5}$$

where r_0 is the anisotropy at $t = 0$, and θ is the rotational correlation time of the sphere [3]. It is important to note that polarization decay can not be modeled with a single exponential function. Several artifacts are responsible for the multiple decay exponents. Scattering of the original polarized excitation source and polarization artifacts of the emission monochromator are significant sources of error for these measurements. The resulting signal has a low signal-to-noise ratio and is very sensitive to even minor polarizer misalignment. The multiple considerations that need to be accounted for are significant when designing an anisotropy based experiment. In the 1970's, a more concise method evolved that measured the diffusion rate of fluorophores into an empty region.

3.2 Fluorescence Recovery After Photobleaching

Fluorescence Recovery after Photobleaching (FRAP) was first reported by Axelrod *et al.*[35] in the 1970's and has become the gold standard in membrane measurements. FRAP consists of staining a membrane or attaching fluorophores to a region of interest. The sample is then viewed under a microscope and is subjected to a high intensity excitation pulse($t = 0$) at the absorption range of the fluorophore. The purpose of which is to effectively destroy a small circular region of fluorophore. As $t \to \infty$, unbleached fluorophore migrates into the area due to the diffusive gradient created. As the sample recovers, the transfer coefficients are determined by plotting the fluorescence intensity as a function of time. The analytical solutions derived allow the differentiation between pure diffusion and convective flow. This is an important result of this research as the two may produce confounding artifacts during data gathering.

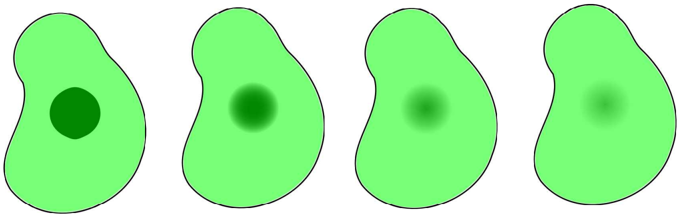

Figure 3.2: Illustration of a typical FRAP experiment. The leftmost figure is at $t = 0$ or immediately after the pulse bleach has been applied. As the spot intensity recovers, the darkened region becomes lighter and lighter. The rightmost figure is for $t \to \infty$. Ideally, all the fluorophore would recover to 100%. Often, experiments have shown this is not the case due to an immobile fraction.

The intensity for a bleached spot at $t = 0$ is a function of the beam profile of the laser that delivers the photobleach. For a uniform circular beam, the fluorescence at $t = 0$ or $F(0)$ is defined as

$$F_k(0) = (qP_0C_0/A)K^{-1}(1 - e^{-K}) \tag{3.6}$$

where, q is a combined quantum efficiency parameter for abosrption, emission, and detector efficiency [35]. P_0 is the total laser power, C_0 is the initial uniform fluorophore concentration, A is the attenuation of beam during recovery observation, and K is a bleach depth parameter. Similarly, the F_0 for a Gaussian beam profile is described in Equation 3.7.

$$F_k(0) = (qP_0C_0/A)K^{-1}e^{-K} \tag{3.7}$$

After the recovery begins, the fluorescence at $t > 0$ is determined by τ_D which is described by the authors as the "characteristic" diffusion time and is defined as $\tau_D = w^2/4D$. As the recovery progresses through time, F_k is driven by τ_D as seen in Equation 3.8.

$$F_k(t) = (qP_0C_0/A)\sum_{n=0}^{\infty}[(-K)^n/n!][1 + n(1 + 2t/\tau_D)]^{-1} \tag{3.8}$$

By combining Equations 3.6, 3.7, and 3.8, the recovery data can be displayed in the fractional form, or normalized by the final intensity value, $F_k(\infty)$, in Equation 3.9.

$$f_k(t) = [F_k(t) - F_k(0)]/[F_k(\infty) - F_k(0)] \tag{3.9}$$

The transfer coefficients can be extracted by fitting the experimental data to Equation 3.9 [35]. FRAP has become the gold standard of membrane viscosity characterization. Since its inception, FRAP was a breakthrough in characterizing cellular components. FRAP has been used to validate the existence of lipid rafts [36], reveal the binding dynamics of the oestrogen receptor [37], and establish the importance of membrane bound protein mobility on gene expression [38]. There is no doubt that FRAP has been an integral tool for the probing of cellular dynamics and physiological processes. This method is not without its own unique considerations. The quality of a FRAP experiment is dependent on meeting a set of ideal assumptions.

Davoust *et al.* [39] reported that the ability to recover the diffusion coefficient is highly dependent on an accurate measurement of the true bleaching radius. Furthermore, Braeckmans *et al.* continued this discussion and established the theoretical framework for FRAP experiments in 3D [40]. Additional considerations include the existence of microdomains and percolation networks [41, 42] which result in a non-uniform diffusion pattern. Within the region-of-interest (ROI), the photobleach pulse may cross-link membrane proteins and increase the local temperature, distorting the true diffusion coefficient [43]. The relatively small area investigated results in a poor Signal-to-Noise Ratio (SNR) [44].

The perfect theoretical experiment would exhibit homogeneous fluorophore concentration, ideal bleach beam geometry, and minimal photodamage, resulting in the optimal lateral 2D diffusion. As clearly stated in Equations 3.6 and 3.7, Axelrod *et al.* [35] assume that τ_D plays no role in determining the initial fluorescence intensity $F_k(0)$. The realistic attainability and limitations of these assumptions will be discussed in the subsequent chapters.

3.3 Molecular Rotors in Membrane Studies

3.3.1 Introduction

The importance of fluorescence anisotropy and FRAP is well established and researched. Both of these methods have a unique set of experimental caveats that make quantitative evaluation of measurements difficult to impossible. Fluorescence anisotropy measurements, in particular, are sensitive to any misalignment or imperfection in polarizing equipment. This consideration applies to both light sources and monochromators. FRAP measurements are subject to striking a balance between good signal-to-noise ratio versus large sample size. FRAP experiments also are costly in time. Given their low spatial and temporal resolution, FRAP experiments are limited in their quantitative capabilities. In recent years, an attractive alternative to both fluorescence anisotropy and FRAP for measuring membrane viscosity has been reported. Molecular rotors have been employed in biological membrane systems as a quantitative method for measuring changes in membrane viscosity [45].

3.3.2 Application

The earliest applications of molecular rotors in membrane systems were focused on vesicles and lipid bilayers. Humphrey-Baker *et al.* [46] reported that indocyanine dye is incorporated into micellar system in aqueous suspensions. Once incorporated, the dye exhibits an increased quantum yield and a blue-shifted emission. Humphrey-Baker *et al.* describe the quantum yield modulation as a function of membrane rigidization as a result of the hydrophobic environment, but detailed explanation of TICT state formation is not given. Kung and Reed performed several spectroscopic studies of DCVJ in both solvents and liposome preparations. A weak linear relationship was established between the solvent's dielectric constant and DCVJ's peak emission wavelength. Kung and Reed [47] found that in a series of solutions ranging from nonpolar (benzene) to highly polar (alcohols), a bathochromic shift of $< 30\,\mathrm{nm}$ was found. The relatively weak shift may be attributed to a lower dipole moment in the LE state than in the TICT state. In the case of non-radiative relaxation, the large shift seen with high dipole moments is not present. A viscosity gradient created with a series of alcohols demonstrated the power-law relationship between viscosity and quantum yield with exponent $x = 0.6$ as described by the Foŕster-Hoffmann equation. Experiments conducted in liposomes prepared from DPPC exhibited a sharp change of the exponent when the temperature was increased over the transition temperature. This behavior highlights the sensitivity of molecular rotors to abrupt changes in free-volume that occurs in the phospholipid bilayer when the temperature enters the transition range between the gel and liquid-crystal phase. The ability to measure the minuscule changes in free-volume that accompany phase transitions highlight the high sensitivity of molecular rotors.

Lukac [48] examined a derivative of (p-(dialkyl1amino)-benzylidene)malononitrile in DPPC and DSPC vesicles and observed a very similar behavior. Lukac found a more pronounced bathochromic shift in DSPC vesicles compared to those formed from DPPC. This was attributed to a different localization in DSPC as a result of the longer tail chains compared to DPPC. Kung and Reed reported the advantage of julolidine based molecular rotors, namely, the separation of polarity and viscosity which only effect peak emission and quantum yield respectively [47]. The use of molecular rotors has been successfully extended to living systems. A review presented by Viriota *et al.* [49] describe applications of conjugated molecular rotors to probe microdomains in polymers, investigate the thermotropic behavior of liposomes, and stain the membranes of endothelial cells. We have investigated the response of membrane viscosity to changes in fluid shear stress. Davies *et al.* [50] report a relationship between shear stress to the activation of G-proteins, but a study with DCVJ-stained cells showed a reversible decrease of membrane viscosity under fluid shear stress [51].

The well-documented use of molecular rotors has given us a wealth of information on which to continue our investigations. Targeted localization of the fluorophore is a consideration for all experiments with biological systems. We have synthesized and characterized molecular rotors with farnesyl chains to aid in the hydrophobic positioning within the membrane [52]. This is the preliminary research that was drawn upon to continue our investigations with molecular rotors and biomembrane systems.

CHAPTER 4

CHARACTERIZATION OF CHANGES IN THE VISCOSITY OF LIPID MEMBRANES WITH THE MOLECULAR ROTOR FCVJ

4.1 INTRODUCTION

The advantages of using molecular rotors to quantify changes in membrane viscosity is well documented[1]. The cell membrane is a highly inhomogeneous complex physical system. Many cellular process such as protein functionality and permeability are influenced by membrane viscosity. Fluorescent probes, and in particular, n-(9-anthroloxy) fatty acids, have been used to explore the relationship between heterogeneity and bilayer depth [53]. These probes have also been used to determine fluidity gradients within the membrane [54]. A central finding of this research is that the apparent viscosity is highly dependent on the placement within the membrane. The regional variations within the membrane highlight the differences between membrane and bulk viscosity. The notion of membrane viscosity is still an effective method for characterizing membrane systems. We have synthesized molecular rotors with hydrophobic tails to aid in the incorporation into the hydrophobic membrane. Namely, we have evaluated the farnesyl ester of the molecular rotor (2-carboxy-2-cyanovinyl)-julolidine [52], referred to as FCVJ. The structure of FCVJ can be seen in Figure 4.1.

---

[1] The research in this chapter has been previously published under Nipper *et al.* [45].

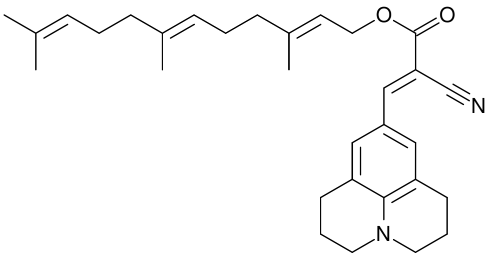

Figure 4.1: Chemical structure of the molecular rotor (2-carboxy-2-cyanovinyl)-julolidine farnesyl ester (FCVJ).

The goal of this study was to incorporate FCVJ into a membrane system. Electroformation giant unilamellar vesicles (GUV) [55] were chosen as the study membrane system. GUVs are widely used and the protocol was ideally suited for the addition of our molecular rotor. The liposomes were exposed to multiple membrane altering agents. Membrane viscosity reducing agents in the form of short chain alcohols were introduced into the liposome system. Conversely, cholesterol and nimesulide was used during the formation process to increase the apparent membrane viscosity. FRAP was used as a secondary technique to corroborate the results of the cholesterol experiments.

4.2 Short Chain Alcohol Experiments

Short chain alcohols have been shown to localize predominantly at the hydrophilic headgroup region of the phospholipid bilayer. The localization results in a disturbance of the natural microsturcture resulting in a decrease in membrane viscosity. Interestingly, the size of the hydrocarbon chain of the alcohol was found to be proportional to the viscosity decrease [56]. This is a prime example of Traube's rule of interfacial tension reduction which predicts that, for every additional methyl group of its hydrocarbon sidechain, the alcohol's ability to reduce the interfacial tension increases threefold [57]. The ability of FCVJ to detect these subtle changes was evaluated. DLPC liposomes combined with FCVJ were exposed to a 2% alcohol series consisting of methanol, ethanol, and propanol. The peak fluorescence intensity was then measured using a spectrophotometer. The relative viscosity was calculated using Equation 4.1,

$$\left(\frac{\eta_2}{\eta_1}\right) = \left(\frac{I_2}{I_1}\right)^{\frac{1}{x}} \tag{4.1}$$

where I_1 is the peak intensity of the control group of of the sample before treatment, I_2 is the peak intensity of the treatment group, η_2/η_1 is the relative change of viscosity, and $x = 0.6$. If background light is negligible and temperature and experimental conditions are identical for all samples, this equation eliminates the constant C described previously in the Förster-Hoffmann equation as well as instrument gain factors. In, Figure 4.2, the relative viscosity is computed as a function of the carbon chain length.

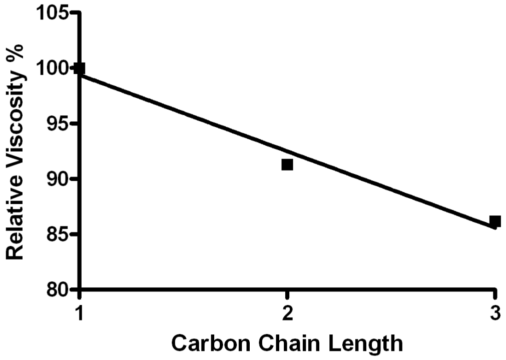

Figure 4.2: Viscosity change as a function of carbon chain length for the alcohols methanol, ethanol, and propanol.

The decreasing viscosity shows a significant linear trend ($R^2 = 0.98$) which is in agreement with Traube's rule. It is believed that this relationship may not hold for longer hydrocarbon chains. The results of this experiment have shown that for an equal concentration, propanol results in a greater reduction in membrane viscosity compared to methanol. Continuing this idea, we set out to examine the effects of alcohol concentration on FCVJ emission. Figure 4.3 shows the response of FCVJ in liposomes to increasing concentrations of propanol.

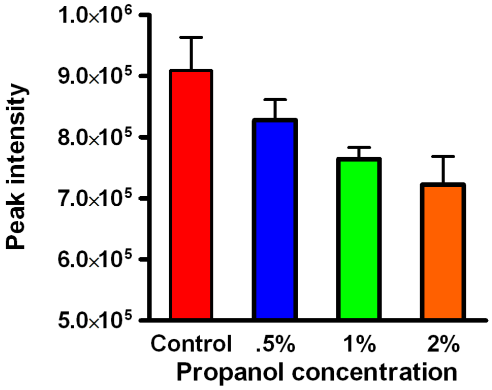

Figure 4.3: Concentration sensitivity to propanol. Even at 0.5%, the decrease in viscosity is significant, compared to the control group. Error bars indicate the standard deviation for N= 4 for each group respectively.

Previous experiments have shown that the alcohol concentration increases the density of the alcohol at the phospholipid surface [56] which in turn reduces the membrane viscosity. Propanol was shown to create the highest change in interfacial energy and was chosen to demonstrate this effect. The relationship between FCVJ and propanol seen in Figure 4.3. As expected, a decrease in intensity is observed as the concentration of propanol increases. This decrease in intensity is indicative of a local decrease in membrane viscosity. Linear regression of the computed viscosity versus propanol concentration exhibit a good correlation ($R^2 = 0.91$), but nonlinear models may better describe the relationship.

4.3 Cholesterol and Nimesulide

Cholesterol plays a role in a number of physiological processes and is a key regulator of membrane viscosity. Cholesterol acts as a partition in the membrane and is expected to increase the viscosity upon integration [58]. Nimesulide is a COX-2 inhibitor commonly prescribed as arthritis medication. The drug disrupts the prostaglandin synthesis production pathway an in turn, acts as an anti-inflammatory agent. The interaction of this drug with the membrane is not well understood [59]. Previous research suggests that the drug has a tendency to migrate towards the inner hydrophobic core of the membrane possibly resulting in a decrease of viscosity. The results of this experiment are shown in Figure 4.4.

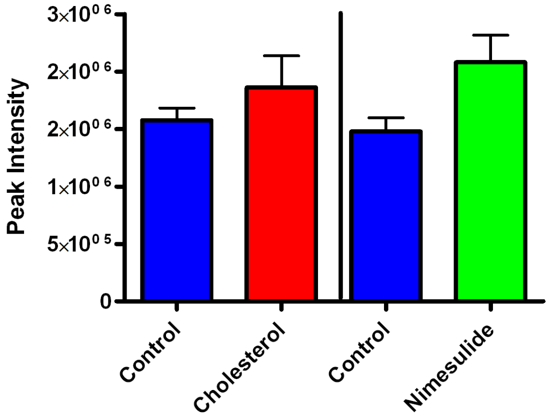

Figure 4.4: Intensity change and computed viscosity change resulting from the addition of the hydrophobic agents cholesterol (left) and nimesulide (right). Cholesterol induced a statistically significant increase in emission intensity of 18% corresponding to a viscosity increase of 32% ($P < 0.01$), whereas the nimesulide induced a 41% intensity increase corresponding to a 63% increase in viscosity ($P < 0.0001$) compared to the control group.

The added cholesterol was shown to induce an 18% increase in intensity (32% increase in viscosity) whereas the nimesulide induced a 41% increase in intensity (63% increase in viscosity). The effects of both the cholesterol and nimesulide were found to be statistically significant with $P < 0.001$ and $P < 0.0001$ respectively. The increases in both viscosity, and resulting intensity, were expected for cholesterol. The conflicting reports on the behavior of nimesulide leaves the results more in question. Previous research suggests that the drug reduces membrane viscosity [60] in contrast to those who report no significant change [61] Recent reports suggest both explanations may be suitable as the effect seems to be concentration dependent. Cholesterol was chosen as the agent for comparison in the FRAP experiments because of the well documented effects on membrane viscosity.

4.3.1 FRAP Experiments

Supported lipid bilayers were formed via vesicle fusion inside PDMS wells adhered to clean glass slides [62]. The lipid bilayers were then incubated in solutions containing 0%, 0.5%, 1% and 2% propanol in water. Additional bilayers were prepared with 15 mol% of cholesterol. FRAP was then performed at 4 different locations. The recovery was monitored and the diffusion coefficient D was calculated using Equation 4.2,

$$D = 0.224 \cdot \frac{r^2}{t_{1/2}} \tag{4.2}$$

where r is the radius of the bleached spot in μm and $t_{1/2}$ is the halftime of recovery of the fluorescence recovery in s [35, 63]. The value of $t_{1/2}$ was obtained through nonlinear regression of the recovery intensity as a function of time with an exponential association. Viscosity is inversely proportional to D [35, 63]. The resulting diffusion coefficients were averaged over the four spots for each concentration. By using the propanol-free medium (0%) as a control, a change in viscosity was calculated for each of the propanol concentrations. Figure 4.5 displays the results of these experiments.

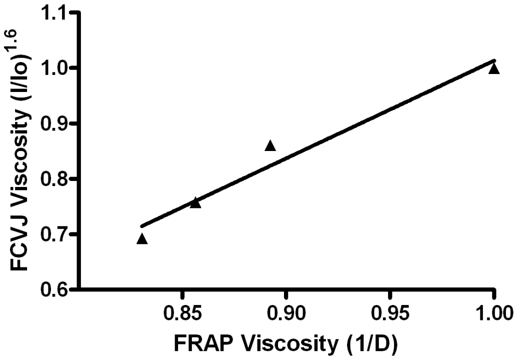

Figure 4.5: Measured viscosity of FCVJ versus FRAP on phospholipid bilayers exposed to propanol concentrations of 0%, 0.5%, 1%, and 2% (v/v). Both methods show a good linear correlation with $R^2 = 0.96$.

FRAP is widely considered the "gold standard" in quantifying membrane viscosity and has proven to be effective. A good correlation ($R^2 = 0.96$) exists between the viscosity dependent FCVJ emission and the FRAP results. Figure 4.4 suggests the FCVJ method is equally effective in quantifying changes in membrane viscosity. When the slope of the correlation is examined, the data suggests that FCVJ may be more sensitive to changes in viscosity relative to FRAP. FRAP experiments report that cholesterol decreases membrane diffusivity by 26% resulting in a calculated increase of viscosity of 36%. This quite similar to the 32% increase reported with FCVJ.

The differences between FRAP and FCVJ are a result of multiple factors. Both methods indirectly measure viscosity and are prone to particular sources of error. FRAP measures the diffusivity of a fluorophore whereas molecular rotors measure the local free volume [23]. The appropriate timescales for these two methods are quite different. FCVJ can respond to changes in the local free volume on the picosecond timescale. FRAP experiments typically require a slow 6-9 minute bleach process followed by a recovery period that may last up to 30 minutes. During the deliberate bleaching process, fluorophore diffusion is continually occurring, effectively lowering the total amount of diffusible fluorophore post bleach. This results in a fluorophore-depleted zone surrounding the bleached spot. This results in a slowing of the diffusive process and this effect is amplified for high diffusivity conditions. This phenomenon may skew the recovery data effectively reducing the sensitivity to changes in membrane viscosity. Finally, FRAP experiments calculate an average diffusivity over a relatively large area (several μM) whereas FCVJ reports physical changes on the molecular scale. Given the heterogeneity of a cellular system, FCVJ is capable of reporting viscosity changes withing membrane microdomains whereas FRAP is limited to averages over relatively large areas.

4.4 Conclusion

FCVJ is an ideal candidate for measuring membrane viscosity. The excellent temporal and spatial response is ideal for monitoring cellular processes. This particular study is a proof of concept for integration into the liposome system. Importantly, FCVJ retained the fluorescent properties required to monitor changes in free volume upon placement in the membrane. Furthermore, the outstanding sensitivity to concentration make this well suited for reactions where substrate or binding is at a minimum. Molecular rotor synthesis can be customized to meet specific experiment requirements such as peak excitation or functional group addition to aid in membrane placement. The flexibility of the molecular rotor system will drive future research efforts. The next immediate goal is to develop strategies in synthesis and instrumentation to correct for variances in fluorophore concentration. Molecular rotors are a relatively new tool that will provide a deeper insight into membrane dynamics.

Chapter 5

Research Goals

We have explored the use of DCVJ derivatives given their affinity towards cellular components. The most noteworthy of these are CCVJ-conjugated phospholipids and FCVJ. The central focus of my research has been to evaluate the efficacy and sensitivity of molecular rotors in biological systems. The foundation of this research was the successful integration of the molecular rotor FCVJ into DLPC membrane systems. Once integrated, FCVJ exhibited sensitivity to changes in the apparent viscosity induced by membrane fluidizing agents. These results were independently confirmed using FRAP experiments. Subsequent to the reporting of this behavior, a new class of ratiometric molecular rotors has emerged.

The first specific aim of this research was to characterize ratiometric molecular rotors in biomembrane systems. Ratiometric molecular rotors are comprised of viscosity sensitive molecular rotor chemically linked to a traditional reference molecule. The advantage of this system is that the dual spectra peaks provided allows for a concentration correction. By dividing the rotor peak by the reference peak, a ratio proportional to the surrounding viscosity is provided. The ratiometric sensing approach will allows to more accurately measure changes in viscosity and account of concentration inaccuracies [64].

The second specific aim of my research is to build and evaluate custom spectroscopic instrumentation for the correction of scattering in biomembrane systems. Fluorescence intensity measurements require the use of high precision instrumentation. The measurement of fluorescence is often impeded by optical imperfections in the sample such as scattering and index of refraction mismatch. This provides a unique opportunity to improve upon the classical design of commercial fluorometers. The design of this instrumentation is intended for future use with ratiometric molecular rotors. The ability to correct for non-ideal optical properties will allow us to more accurately quantify viscosity changes.

The final specific aim is to create and evaluate a FRAP simulation for the optimization of confocal-based diffusion experiments. FRAP is the most widely used and well documented method for quantifying membrane viscosity. We intend to highlight the unique advantages of pre-experiment optimization. Furthermore, the open source nature of this simulation will allow us to create a calibration data set for the evaluation of commercial closed source data analysis algorithms. The future use of this research is to independently confirm the viscosity measurement capacities of molecular rotors. Also, the ability to compare and contrast different methods will aid in the evaluation of molecular rotors as membrane viscosity reporters. The following three chapters of this dissertation are prepared in accordance with the manuscript style format.

CHAPTER 6

QUANTIFICATION OF MEMBRANE VISCOSITY WITH RATIOMETRIC MOLECULAR ROTORS

6.1 INTRODUCTION AND THEORY

Membrane viscosity is a characteristic term that describes the ease of movement within the phospholipid bilayer [58]. Recently, membrane viscosity has been investigated as a possible approach to indicate physiological processes within the cell [65, 66, 67, 27]. Membrane protein functionality and in particular, carrier mediated transport and membrane bound receptors, are directly influenced by membrane viscosity [32, 26]. Increases in membrane viscosity have been reported with the onset of atherosclerosis [67], malignancy [25], diabetes [29, 30], and hypercholesterolemia [28]. Conversely, a decrease in membrane viscosity has been linked with amyloid precursor protein production in patients with Alzheimer's disease [31]. Probing and quantifying changes in membrane viscosity may prove to be an exceptional tool to cell biologists and clinicians alike.

Mechanical methods such as magnetic based rheometry and micropipette aspiration both transduce a physical measuring force which may impact the physiological state of the membrane. Both micropipette aspiration and magnetic rheometry return averaged values for a large region and can not reveal local variances. Furthermore, these methods are surface based and are unable to characterize inner core dynamics of the membrane. Because of these considerations, these methods are also limited in both temporal and spatial resolution. Fluorescence based methods have become the gold standard for measuring membrane viscosity over the past 30 years. The most well established and documented methods are fluorescence anisotropy and fluorescence recovery after photobleaching (FRAP). Fluorescence anisotropy measures the polarized emission upon excitation of a special class of fluorophores. Depolarization is dependent on rotational diffusion which is a function of the local viscosity. Anisotropy experiments are subject to significant sources of error. Irregular polarization tendencies of both the excitation and emission stages of the instrumentation are significant sources of error. An alternative to anisotropy is FRAP.

FRAP experiments are widely used to characterize particle movement within the membrane. This is achieved by irreversibly photobleaching a population of fluorophores within a membrane, monitoring the diffusive recovery of intact fluorophores, and computing the rate constants for the recovery. The resulting rate constants are directly proportional to the solvent viscosity. FRAP is widely used and has been used to evaluate the influence of membrane bound protein mobility on gene expression [38]. Both fluorescence anisotropy and FRAP are have unique considerations when designing an experiment.

An alternative to the traditional fluorescence based methods has emerged in recent years. Molecular rotors are a unique class of fluorophores that exhibit a free volume dependent quantum yield. This sensitivity results from a bimodal deexcitation path distributed between traditional radiative photon release and a torsional twisting force. The rotation of these molecules are directly impeded by free-volume, which is a function of the bulk viscosity properties. This behavior allows the inference of viscosity properties by measuring changes in the quantum yield. The Förster-Hoffmann equation shown below establishes the dependency of the quantum yield ϕ_F on the local viscosity η,

$$\log\phi_F = C + x \cdot \log\eta \tag{6.1}$$

where C and x are proportionality constants and typically $x = 0.6$ resulting in a unitless quantification. Because fluorescence emission is proportional to the quantum yield, simple emission intensity measurements are an adequate method for probing the local microviscosity. Previous research efforts have focused on single emission (2-carboxy-2-cyanovinyl)-julolidine (CCVJ) derivatives. In particular, a farnesyl linked CCVJ derivative, abbreviated FCVJ, has been shown to exhibit local viscosity dependent quantum yield [45]. The structure of FCVJ is shown in Figure 4.1.

The intrinsic rotation of the molecular rotor can be observed around the cyanovinyl group near the julolidine. The long farnesyl tail is a purposefully placed hydrophobic region that is meant to encourage incorporation into the similar hydrophobic tail region within the membrane. We have successfully incorporated FCVJ into a liposome model system and evaluated the effects of short and long chain alcohols, cholesterol, and various pharmaceutical compounds on membrane viscosity. Furthermore, FRAP experiments with increasing concentrations of cholesterol were used to compare the viscosity sensing capabilities. This method provided a fluorescence intensity based method for quantifying changes in apparent viscosity. One limitation of this approach is the sensitivity of viscosity measurements to concentration inaccuracies.

Fluorescence intensity is primarily dependent on the concentration of fluorophore. A family of ratiometric based molecular rotors have been synthesized and provide a strategy for correcting skewed viscosity measurements from concentration inaccuracies. Ratiometric molecular rotors are comprised of non-viscosity sensitive reference fluorophore conjugated to a traditional molecular rotor. In a traditional viscosity gradient experiment, as the viscosity increases, the rotor peak continues to increase whereas the reference peak remains relatively stable. By dividing the variable rotor peak by the more constant reference peak, a ratio that describes a baseline viscosity reading is calculated. The dual emission spectra that comprises these fluorophores is able to be altered in a way to bring a balance of reference and rotor signal. The length of the linker chain between the two portions is of great importance and we have evaluated 4 iterations of this scheme. The multiple fluorophores tested in this study are shown in Figure 6.1.

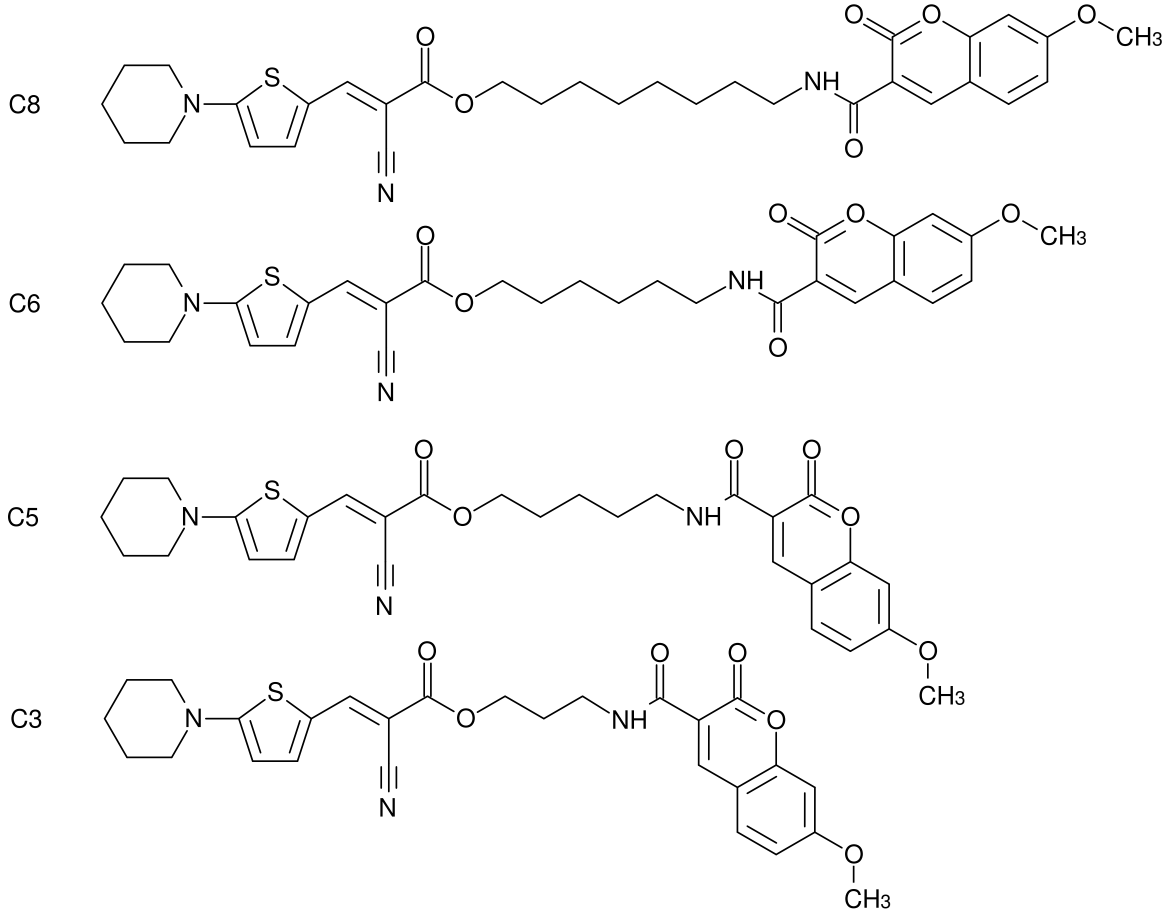

Figure 6.1: Chemical structures of the molecular rotors C3, C4, C5, and C6 used in this study. Coumarin is used as reference for these dyes and can be found on the rightmost side of the molecules. The coumarin is linked with a variable size carbon chain to a thiolphene group (left) which is the viscosity sensitive molecular rotor .

The first goal of this study is evaluate and characterize the viscosity sensitivity of the dyes shown in Figure 6.1. Next, the dyes will be integrated into a liposome model and the response to propanol will be studied. The ratiometric molecular rotor that exhibits the highest sensitivity to propanol will be further examined to test the resolution and sensitivity to changes in propanol concentrations. Upon incorporation into a membrane, it is our objective to determine the optimal emission spectra as a function of the linker size. The final objective of this study is to assess the concentration independence of the ratiometric sensing system.

6.2 Materials & Methods

6.2.1 Viscosity Gradient

The viscosity sensitivity of the ratiometric dyes evaluated were established in gradient experiments with ethylene glycol and glycerol. Excitation scans are first performed on the lowest viscosity sample in the spectrophotometer (Jobin-Yvon). The optimal excitation wavelength is then used throughout the gradient experiment. This step is performed to provide a uniform standard for the fluorophore's sensitivity to changes in bulk viscosity. This also serves the dual purpose of observing the non-viscosity sensitive reference and the molecular rotor spectra. From the peak rotor emission spectra recorded, the peak will be plotted as a function of viscosity and the sensitivity will be computed.

6.2.2 Liposome Formation

All agents and alcohols were purchased from Sigma-Aldrich unless otherwise stated. The ratiometric molecular rotors were synthesized by our own group [68]. A 10 mM stock solution of each rotor was prepared in chloroform. 4 μL of each stock was added to 200 μL of DLPC:chloroform (Avanti Polar Lipids) in a glass vial. An established electroformation process was used to create unilamellar liposomes [55, 69]. Prior to formation, the platinum electrodes were sonicated and cleaned in Alconox detergent and ethanol respectively. A glass syringe was used to deposit the rotor/DLPC mixture onto the platinum electrodes. The chamber was placed under vacuum for 30 minutes to remove any remaining organic solvents. Glass coverslips were placed over the top of the chambers to prevent outside impurities from entering. The chambers were then flooded with 10ml of a 250 mM sucrose:double distilled water solution. The electroformation process was started by applying a 1 V_{pp}, 10 Hz sinusoidal signal to the two electrodes for 10 minutes. The frequency was then lowered to 1 Hz for 5 minutes. The contents of the chambers were then extracted using a sterile syringe (BD) and an electrode rinsing process. The final liposome/sucrose suspension were then stored in a clean tube at 10°C for no more than 24 hours.

6.2.3 Short Chain Alcohol Sensitivity and Gradient

A volume of 500 μ L of liposome/rotor suspension was added to 500 μ L of either 250 mM sucrose or a 10% Propanol/250 mM Sucrose solution for each ratiometric rotor evaluated. Propanol was chosen to meet an optimal balance of interfacial energy and solubility. N= 10 was chosen for each group to ensure statistical robustness. The solution was then gently inverted 5 times and placed into a temperature controlled turret (Quantum Northwest) set at 10°C and equilibrated for 5 minutes. The sample was then excited at 352 nm in the spectrophotometer (Jobin-Yvon) and spectra was gathered for a range of 370-520 nm with slit settings of 5. The peak intensities from all graphs were normalized to their respective means and graphed. The ratiometric dye with the highest sensitivity to the Propanol solution was chosen and a gradient experiment was conducted. Five concentrations of Propanol (v/v)% were chosen with 4 repeats to improve robustness. The same spectrophotometer settings were applied and both the reference and rotor peaks were analyzed.

6.2.4 Data Analysis

Data analysis was performed on the spectra for all sets. The ratiometric data was calculated by recording the peak intensity at 479 nm, the viscosity sensitive rotor peak, and dividing by the non-viscosity sensitive reference peak at 410 nm. To compare the peak intensities the sets were normalized by the mean intensity. The groups were then compared via the Students t-test to confirm a statistically significant difference. The bar graphs show the normalized mean and the error bars represent standard deviation. All data analysis was performed with Graphpad PRISM version 4.01.

6.3 Results & Discussion

The first experiment set is a bulk solvent viscosity gradient in mixture of ethylene glycol and glycerol. The purpose of this set is to analyze the balance between the reference fluorophore and the molecular rotor portion. It is important to confirm for the ratiometric dyes that the reference dye is indeed non-viscosity sensitive and conversely evaluate the rotor sensitivity. These spectral scans reveal information about the dye structure and the effects of manipulating the length of the linker chain between the two fluorophores. In Figure 6.2, the spectral scan of the ratiometric rotor C3 reveals a dynamic balance between the reference and the rotor. This protocol was repeated for all ratiometric dyes characterized.

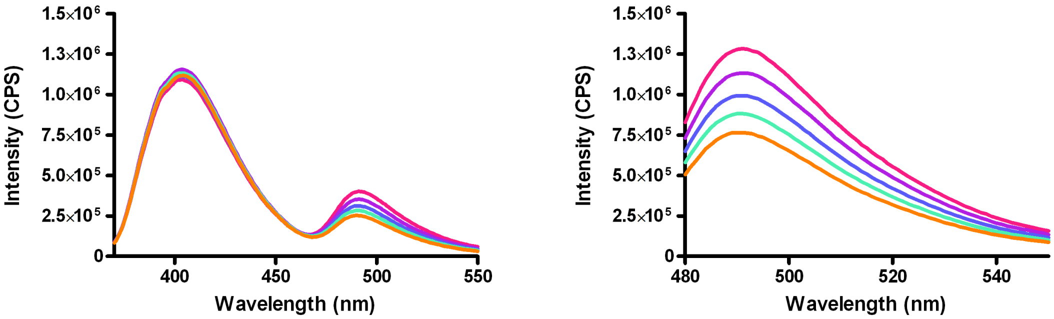

Figure 6.2: Single point reference (left) and rotor(right) emission scans of C3 in etylene glycol and glycerol gradient. In the reference excitation graph, the low variability of the reference relative to the rotor emission (≈ 410nm) highlights the ratiometric properties. The rotor excitation graph confirms the viscosity sensitivity of the molecular rotor.

In Figure 6.2, the left graph is the single point UV excitation. It is believed that for these ratiometric dyes, a resonance energy transfer is occurring between the reference and rotor. This is accepted due to the distance (nm) of UV light ($\approx 350nm$) from the optimal excitation spectra for the rotor ($\approx 470nm$). For C3, in the left graph the higher intensity peaks around 410 nm is the reference peak. The second variable peak is the viscosity sensitive molecular rotor portion of the molecule. The graph to the right is the direct excitation of the rotor with an excitation of $470nm$. To confirm the rotors sensitivity to viscosity, the log of the peak intensity for both the reference and the rotor is plotted as a function of the log viscosity. The purpose of this is to confirm rotor sensitivity and to evaluate reference stability. Figure 6.3 shows the sensitivities of both the reference and rotor to changes in viscosity.

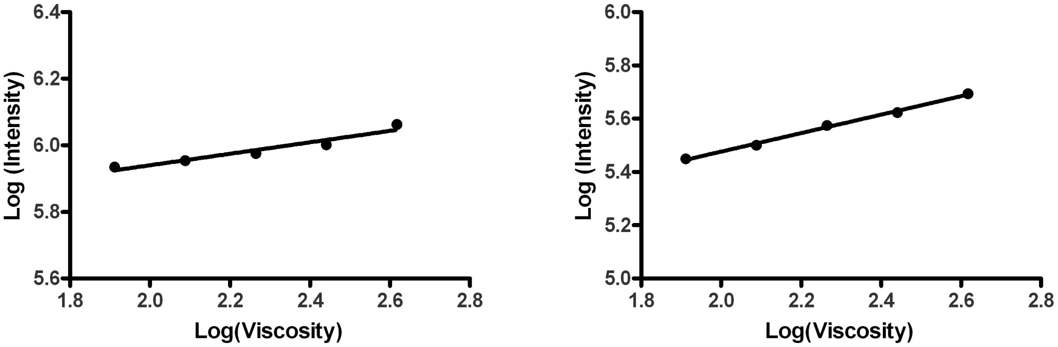

Figure 6.3: Plot of the C3 peak emission from the single excitation measurement in Figure 6.2. The linear correlation for the reference(left) and the rotor(right) are $R^2 = 0.9299$ and $R^2 = 0.9962$, respectively. The slopes for the reference and rotor are 0.1717 and 0.3466 respectively.

This experiment confirms that the molecular rotor portion of the C3 dye is indeed sensitive to changes in viscosity. One important observation is that the reference portion also appears to response to changes in viscosity. While the trend is statistically significant, the sensitivity is low in comparison to the rotor. One possible explanation for this phenomenon is the changing refractive index of the solutions as the glycerol concentration is increasing. As described in the previous chapters, the permitivity directly influences the quantum yield and subsequent fluorescence emission. The advantage of having the reference and rotor emission spectra is that it allows for a concentration correction. By dividing the rotor peak by the reference peak, a unitless ratio is calculated that acts to normalize data that may have variations in concentration. Figure 6.4 is the ratiometric calculation for the C3 viscosity gradient plotted in Figure 6.3.

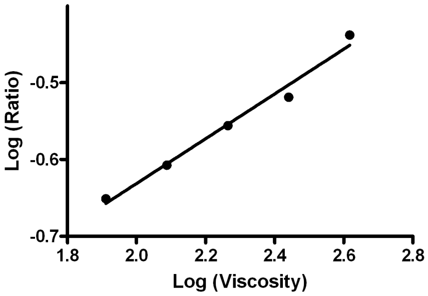

Figure 6.4: Calculated ratio versus viscosity of C3. The peak rotor emission divided by the reference emission for C3 in ethylene glycol and glycerol. The log was computed for both the viscosity and ratio and then plotted. A slope of 0.2917 with a significant linear correlation ($R^2 = 0.9821$) was calculated. These values were taken from the reference excitation spectra in Figure 6.2.

The significant linear trend in Figure 6.4 confirms the response of the ratiometric plot to changes in viscosity. The heightened sensitivity range, as shown by the increased slope, is important because it allows for a better signal-to-noise ratio. The ability to divide the rotor emission by the reference emission allows researchers to extract a more accurate viscosity measurement compared to the traditional intensity-only measurements. The behavior in a bulk solution compared to the phospholipid environment of the liposomes can often be quite different. To determine the most effective ratiometric rotor within the liposome, each rotor was formed within the DLPC liposome protocol. From here, each group was separated into 2, N= 10 groups; 1 control group and 1 experimental group comprised of a 50/50 liposome and 5% propanol/sucrose solution. The ratiometric calculations of the rotor peak divided by the reference peak were then computed. A percent change in ratio were then computed as seen in Figure 6.5.

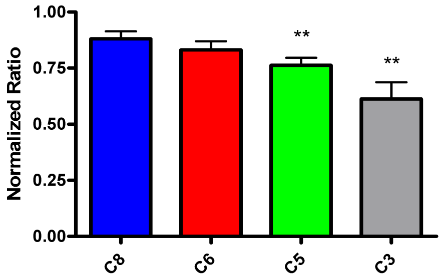

Figure 6.5: Normalized intensity change in percent for ratiometric dyes incorporated in DLPC liposomes. All groups were treated with a 5%(v/v) propanol to sucrose solution with N= 10. ANOVA followed with a Dunnet's test analyzed the difference in means between the groups. For the Dunnet's test, the C8 group was chosen as the control and the following groups were compared. The asetricks represent $P < 0.01$, which confirms a high statistical difference between the means of the control and experimental groups respectively. C6 did not exhibit a statistically significant difference compared to the C8 control group.

From Figure 6.5, the C3 dye showed the highest change in ratio in response to the propanol treatment. This is important in establishing the sensitivity post liposome incorporation. The increased sensitivity appears to be in direct correlation with the linker size that joins the two dye molecules. This increased sensitivity is most likely due to an increased resonance energy transfer efficiency under the single point excitation. As the linker becomes smaller, the energy transfer efficiency is increased, and changes in the rotor emission are more pronounced. To test the resolution of this sensitivity, we created a propanol gradient with 5 increasing concentrations of propanol in sucrose solution. Figure 6.6 is an example of the response of the C3 dye to the propanol treatment.

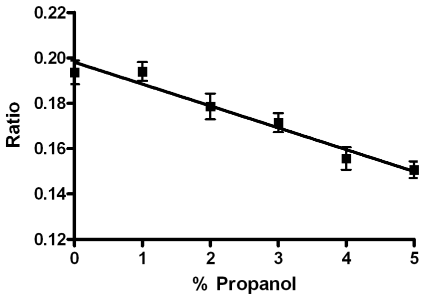

Figure 6.6: Ratio of the peak rotor emission to the reference emission for C3. The C3 liposomes were exposed to increasing concentrations of propanol. Propanol was chosen to achieve the maximum interfacial energy without destroying the membrane. The linear response of the ratio is indicative to a viscosity sensitivity for the liposome group.

Figure 6.6 suggests the successful incorporation of the C3 into the phospholipid membrane. Furthermore, the C3 dye retains the intrinsic sensitivity to changes in viscosity upon incorporation. Propanol was chosen for these experiments because of the higher interfacial energy respective to the membrane. The excellent dose response continues a trend established with FCVJ as seen in Figure 4.3. The significant trend demonstrates the ability of the ratiometric technique to report minuscule changes in the local viscosity of the phospholipid membrane.

6.4 Conclusions

We have demonstrated the viscosity sensitive characterization of a ratiometric dye and incorporated the fluorophore into a liposome biomembrane system. Furthermore, we have shown the sensitivity of the molecular rotor once incorporated and tested the robustness of ratiometric testing techniques. Molecular rotors have an almost instantaneous response to changes in the local viscosity along with a high spatial resolution. Molecular reporters have previously been shown to monitor conformational changes in proteins, polymerization dynamics, and membrane viscosity. The immediate challenge for molecular rotors is to move from the liposome model into cell culture. Early toxicity studies with DCVJ have proven cell viability with low concentrations. The next phase of this research is to identify and characterize the ideal ratiometric molecular rotor, and move to cell culture experiment. Previously reported intensity-only based methods using molecular rotors were limited by fluorophore concentration inaccuracies. The ratiometric sensing techniques opens the door to a new realm of viscosity based reporting modalities.

CHAPTER 7

FLUOROPHOTOMETER WITH CORRECTIVE STRATEGIES FOR INTENSITY BASED MEASUREMENTS

7.1 INTRODUCTION

Membrane viscosity is a term used to quantify the ease of movement within the phospholipid bilayer [58]. Membrane viscosity has been identified as a possible indicator of cellular physiology [65, 66, 67, 27]. A significant portion of these molecules experience changes in membrane-bound protein mobility. Protein mobility is a direct function of membrane viscosity. Increases in membrane viscosity have been reported with the onset of atherosclerosis [67], malignancy [25], diabetes [29, 30], and hypercholesterolemia [28]. Conversely, a decrease in membrane viscosity has been linked with amyloid precursor protein production in patients with Alzheimer's disease [31]. Quantifying membrane viscosity may be a useful indicator for the onset of the disease state in the cell.

Fluorescent methods are the ideal reporters for measuring membrane viscosity because of their high spacial and temporal response. With lifetimes on the 10^{-9}s timescale, molecular rotors can report minuscule changes in viscosity on an almost instantaneous timescale. Molecular rotors are a unique class of fluorescent reporters that exhibit a photoinduced rotation. This intramolecular rotation competes with fluorescence emission for the preferred deexcitation pathway. The local free volume directly influences the ease of rotation. Changes in bulk viscosity result in the expansion or contraction of free volume. Molecular rotors can sense and report changes on the molecular level which are proportional to bulk solution property changes. The viscosity dependent quantum yield exhibited by molecular rotors is described by the Förster-Hoffmann equation which is shown in Equation 7.1

$$log\Phi_F = x \cdot log\eta + C \tag{7.1}$$

where Φ_F is the quantum yield, η is the solvent viscosity, C is a general constant, and x is described as a dye-dependent constant with a maximum value of 0.6. The log-log relationship between quantum yield and solvent viscosity provides an accurate means to examine the physical environment surrounding the molecular rotor. Recently, we have reported the use of molecular rotors to examine the viscosity of biomembrane systems [45].

The accuracy of these viscosity measurements, in membrane systems, is dependent on the ability of measuring the average fluorescence intensity of the sample in question. The quantification of intensity based measurements are confounded with non-ideal optical properties of the dye containing solution. Fluorescence requires the absorption of excitation light and the parameter used to describe this property is termed the molar extinction coefficient. Additional absorption of light from non fluorescing species may occur during the experiment. Measuring the true absorbance is necessary if quantifying the true quantum yield is desired. Inaccuracies arising from the scattering properties of a sample may lead to non-optimal quantification of fluorescence intensity. This behavior arises from the impedance of excitation light and redirection of the subsequent fluorescence emission.

The ability of molecular rotors to reveal the physical properties of the local environment is dependent on an accurate sampling of the quantum yield for the entire reporter population. Scattering and multiple absorbing species make this task more complicated. By employing different correction schemes, we expect to account for these effects and improve the measured quantum yield. Commercial base model spectrophotometers are not commonly found with these features, and models with the correction capabilities are cost prohibitive. We have constructed a spectrophotometer that allows the correction of non-fluorescence absorption and the optical turbidity of a fluorescent sample. This custom built device is optimized for the purpose of reporting fluorescence based viscosity measurements with molecular rotors, and is referred to as a fluoroviscometer.

7.2 Materials and Methods

7.2.1 Fluoroviscometer

The main control platform is built on an embedded Pic18F8520 microcontroller. The control center converts the analog signal supplied from the photomultiplier tubes into a digital signal. The applied gain is also delivered to both the excitation and emission detection hardware. The local user interface is established with a keypad and LCD screen(Optrix). The excitation unit is comprised of a 405 nm (deep blue) laser diode, a 532 nm (green) laser diode and a 352 nm (ultraviolet) LED. The blue and green laser diodes are focused through the use of a dichroic mirror into an aspherical collimator (Thorlabs) which is connected to one end of a bifurcated optical fiber (Oceanoptics). The other end of the bifurcated fiber receives the free space collimated UV light. As the excitation light exits the fiber, its is collimated and power fluctuations are monitored using a 90/10 mirror positioned at a 45° into a photodiode (Thorlabs). Additional lenses are used to further focus the light as it enters the sample. A temperature controlled 4 position turret (Quantum Northwest) with an an adjustable Z-stage (Thorlabs) is used to locate the sample. Fluorescence spectra is gathered $\perp$ to the excitation source using a monochromator unit from a SPEX Fluorolog 2 fluorophotometer. A photomultiplier tube (PMT) is used to quantify the fluorescence intensity. The absorption is measured $\|$ to the the excitation light path. A neutral density filter is placed in front of a powered photodiode to measure the absorbance of a sample. A sketch of the system is shown in Figure 7.1.

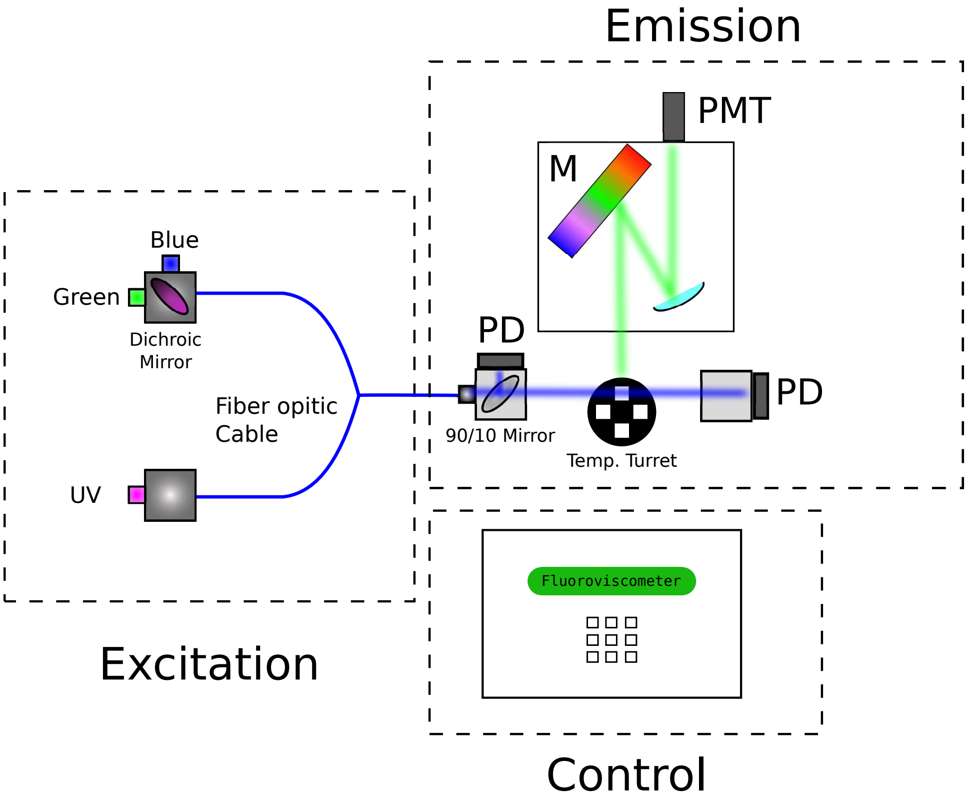

Figure 7.1: Schematic of fluoroviscometer excitation, emission, and control units. The flexibility of the fiber optic y-cable in the excitation unit allows for the interchanging of excitation units. The current excitation unit is comprised of 405 nm and 532 nm laser modules collimated into one end of the fiber whereas the other end collimates the UV LED. The 90/10 mirror focuses into a photodiode (PD) to provide power monitoring for reference correction. The straight path PD measures the absorbance of the sample. The sample is held in temperature controlled turret for environment consistency. All measurement signals are processed and controlled in the local control unit.

The fluoroviscometer is controlled via a control program written in C language. The RS-232 serial communication protocol is used to communicate between the controller and the software user interface. The user software allows for the independent excitation of the 365 nm (UV), 405 nm (Blue), and 532 nm (Green) diodes. The emission monochromator can be positioned at any wavelength if a particular emission point is of interest. Additional filters can be added to the photodiode if a specific absorption wavelength is desired. The ability to automate and average scans also improve the accuracy of spectral measurement. Background subtraction and reference correction are also implemented so as to provide a more accurate signal. A snapshot of the control software can be seen in Figure 7.2

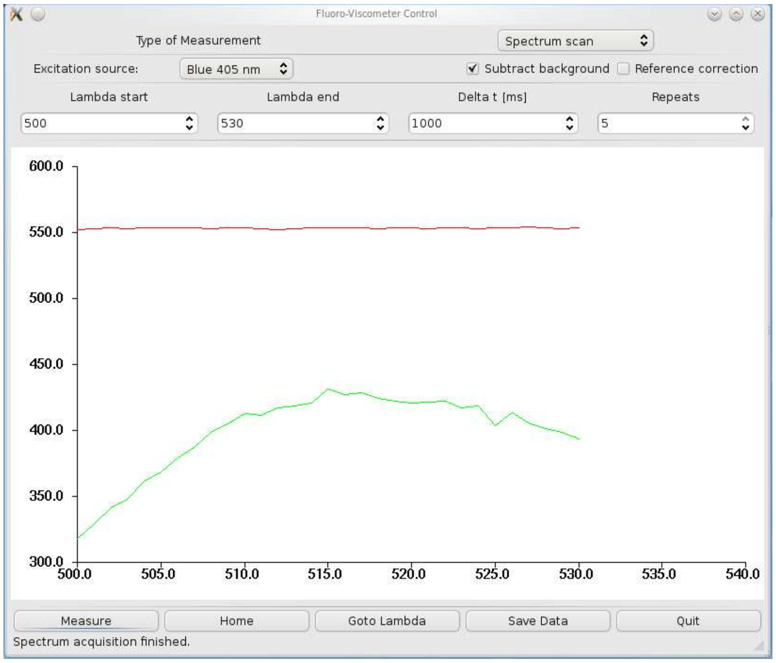
Fluoro-Viscometer Control

Type of Measurement: Spectrum scan

Excitation source: Blue 405 nm

☑ Subtract background ☐ Reference correction

Lambda start: 500

Lambda end: 530

Delta t [ms]: 1000

Repeats: 5

Spectrum acquisition finished.

Figure 7.2: Screenshot of the fluoroviscometer software user interface. The green line is the average peak spectra for Lucifer Yellow (PBS) excited under 405 nm laser. The red line is the straight channel photodiode that is used to calculate the absorbance.

7.2.2 Sample Evaluation

Lucifer yellow was used as a test fluorophore to compare the response of the fluoroviscometer to a traditional fluorophotometer. Lucifer yellow was chosen because of the high quantum yield, high water solubility, and adequate absorption spectra in the 405 nm range. A concentration gradient from 0.05μM to 0.75μM in double distilled water was prepared and used for the fluorescence and absorbance evaluation experiments. The capabilities of absorbance measurement were evaluated and compared to a traditional UV-Vis spectrometer (Beckman).

The spectrometer reports the optical density in unitless absorbance. For consistency the absorbance A_λ, measurements for the fluoroviscometer were calculated using Equation 7.2,

$$A_\lambda = -\log_{10}\left(\frac{I}{I_0}\right) \tag{7.2}$$

where I_0 is the intensity of a blank sample of PBS containing no fluorophore, and I is the intensity for a given concentration of Lucifer Yellow. The scattering correction was evaluated by using a constant concentration of lucifer yellow with increasing amounts of 1μm polystyrene beads (Polysciences).

7.3 Results and Discussion

The first set of experiments were to confirm the ability of the fluoroviscometer to detect a fluorescence signal. A concentration increasing gradient of lucifer yellow in water was prepared and tested. Figure 7.3 confirms the response of the device to an increasing fluorescence signal.

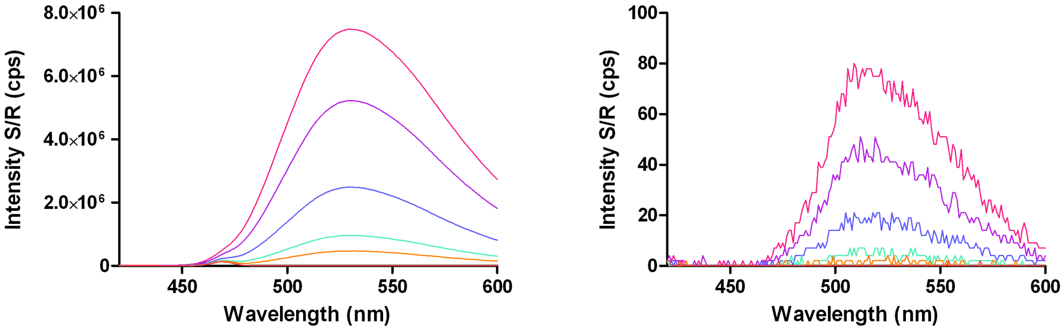

Figure 7.3: The spectral response of the fluoromax(left) is evaluated with the lucifer yellow concentration gradient. The fluoroviscometer is tested with the same sample set and the spectra is shown (right).

The spectral response of the fluoroviscometer (FVM) is quite similar to that of the commercial spectrophotometer. One obvious feature of the FVM spectra is the high amount of noise within the signal. The signal levels for this particular experiment are quite low. There are several possible points of control in this device that may result in the noisy signal. Among these, are two separate controllable slits on the emission monochromator, proper focusing of the emission light onto the monochromator, and the adjustable photomultiplier tube settings. Adequate excitation light intensity is essential for a high emission signal and considerations through the optics, such as light loss and focusing, all contribute to the quality of signal. To examine the accuracy of peak measurement, the peak intensity was plotted as a function of molar concentration of lucifer yellow for both the commercial spectrophotometer and the fluoroviscometer. Figure 7.4 highlights the results of these experiments.

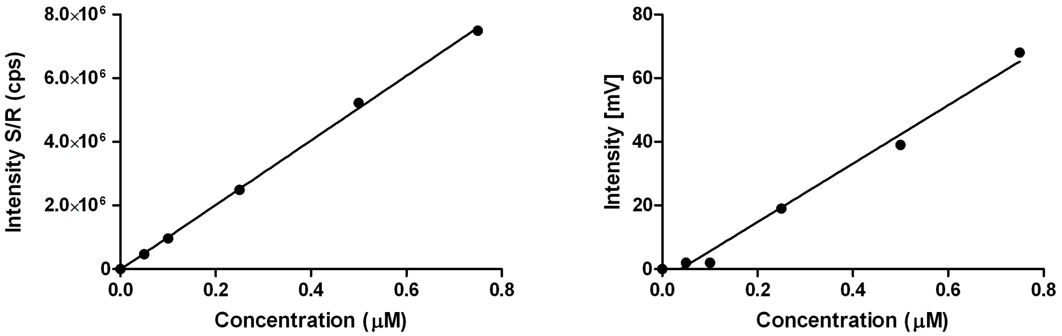

Figure 7.4: The fluorescence signal peak was taken at 530 nm for both instruments and plotted against the concentration. The fluromax (left) shows a high linear correlation ($R^2 = 0.9990$). The fluoroviscometer also shows a statistically significant trend($R^2 = 0.9877$) of fluorescence versus molar concentration.

As Figure 7.4 confirms, a significant linear trend is present for the fluoroviscometer as a function of molar concentration of lucifer yellow. The validity of this device has been established. The fluoroviscometer contains many features that are absent in common commercial spectrophotometer. Often, fluorescence measurement is impeded at high concentrations due inner filter effects. One possible strategy for accounting for high concentrations is to measure the absorbance of excitation light. Our device is equipped with a photodiode positioned along the excitation path directly behind the sample. This allows for the absorbance of the sample to be measured. The same gradient used in the fluorescence validation experiments were used to evaluate the absorbance measurement capabilities. A traditional UV-vis spectral analyzer (Beckman) was used for comparison as seen in Figure 7.5.

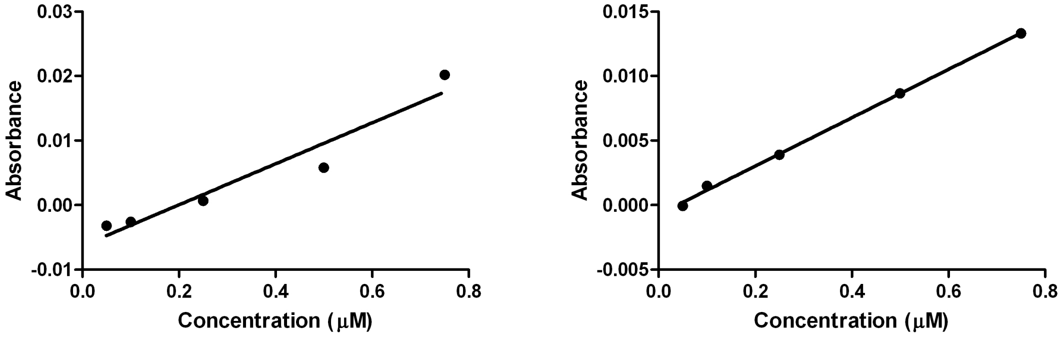

Figure 7.5: The absorbance capabilities of the commercial UV-Vis (left) are compared to that of the fluorovicometer (right). A gradient of lucifer yellow (PBS) with the same molar concentration used in Figure 7.3 was used to evaluate the two instruments

Figure 7.5 compares the absorbance capabilities of the UV-Vis to that of the fluoroviscometer. The UV-Vis reports a significant linear trend ($R^2 = .9330$) for absorbance versus molar concentration. The same experimental set tested in the fluoroviscometer yielded a correlation of $R^2 = .9983$. The UV-Vis was unable to detect low concentrations of fluorophore in the solution. The fluoroviscometer had no problems with evaluating low concentrations as shown in Figure 7.5.

Absorption by fluorophore is not the only cause of a reduction of intensity post-sample. The optical qualities of the sample such as index of refraction and turbidity are important considerations. The fluoroviscometer is equipped with features that can be used to quantify the turbidity of a sample. By choosing a scattering wavelength that is well away from the absorption band of a fluorophore, a sample can be illuminated with a "scattering excitation", in our case a 532 nm (green) laser diode. The scattering wavelength is then measured ⊥ to the excitation path. As the optical turbidity increases, the amount of scattered green light increases. This feature was validated in the fluoroviscometer by measuring a scattering gradient set. A constant molar concentration of 1 μmol Lucifer Yellow was dissolved in PBS and increasing amounts of 1 μM polystyrene beads were placed in the sample. The scattering properties were then investigated by collecting and comparing both the fluorescence peak of the Lucifer Yellow and the non fluorescent scattering peak. The results are shown in Figure 7.6.

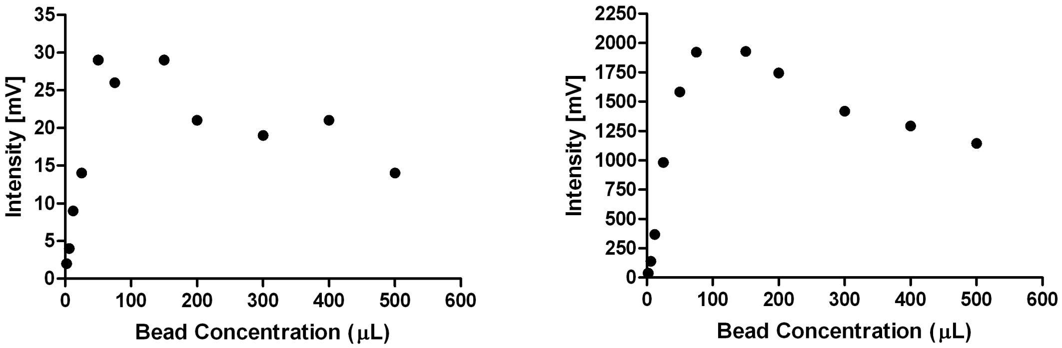

Figure 7.6: Peak intensities from both the fluorescence (left) and scattering (right) signal measurements recorded by the fluroviscometer. Both the fluorescence and scattering intensities initially rise and then begin to decrease.

As Figure 7.6 shows, by increasing only the non-fluorescing scattering agents, the measured fluorescence intensity increases. This is a result of the fluorescence emission being randomly distributed in all directions, including ⊥ to the excitation path. The balance begins to shift as the scattering agent continues to increase. At these higher concentrations, the excitation light is impeded and the the population of excited fluorophores begins to decrease. Similarly, the intensity of the scattering wavelength continues to increase but begins to decline at higher concentrations. It follows that the scattered light distribution is initially increased in all directions. As the bead concentration increases, the green light can not evenly penetrate the sample and the measured light declines. Scattering is a serious consideration if the fluorescence intensity is the primary means of detection. If the scattered light response could be quantified and modeled, a corrected fluorescence measurement could be made. One strategy is to examine the correlation between peak fluorescence emission and scattered light exists. Figure 7.7 shows a linear correlation of the scattered intensity vs. the peak fluorescence intensity.

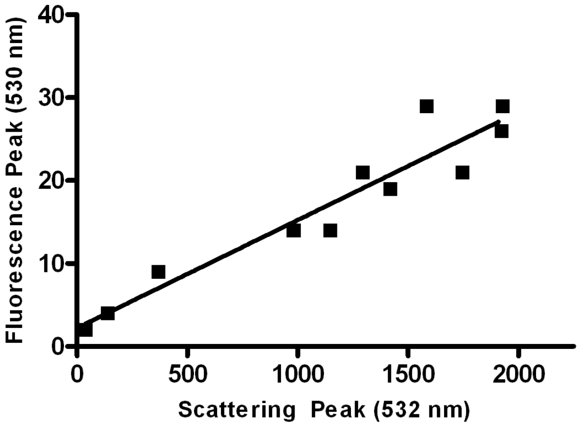

Figure 7.7: Correlation of the fluorescence signal($R^2 = 0.9095$) as a function of the scattering signal.

The trend in Figure 7.7 is statistically significant with a considerable amount of standard deviation. Improving the collection of fluorescence signal through instrument settings and optical alignment will improve the signal-to-noise ratio. Given the digitization range for the data, $0 - 2497$, considerations of PMT gain and slit settings must be made. These settings must be accommodated so as to gather the entire range of samples without reaching the lower or upper threshold. In these regions, the PMT begins to exhibit a non-linear response. This is a major consideration, and one future research will attempt to remedy.

7.4 CONCLUSIONS

We have presented a fluoroviscometer that is capable of measuring both absorbance and scattering in a addition to fluorescence emission. The non-ideal optical properties prohibit accurate quantification of the true fluorescence signal. In samples containing phospholipids, such as liposomes, the scattering content increases as a function of the lipid concentration. By measuring both the sample scattering and the absorbance, an improved signal is possible. Advances in experiment optimization will increase the signal-to-noise ratio necessary for scattering correction. The next step of this research is to develop improved strategies for the correction of scattering. We plan to further characterize the role of scattering by evaluating the effects of size, concentration, and media on the scattering properties. The ability to derive a clean signal will prove a valuable asset for fluorescence based experiments.

Chapter 8

Open Source FRAP Simulation for the Evaluation of Closed Source Algorithms

8.1 Introduction

Fluorescence Recovery After Photobleaching (FRAP) is a tool widely used by cell biologists for studying fluidity of cellular components. FRAP measures the diffusivity of a medium by measuring the rate of diffusion of a known fluorophore. Diffusion coefficients are determined by staining a membrane with a fluorophore or attaching the fluorophore to a mobile cellular structure. After the fluorophore is in place, a small spot is photobleached on the region of interest (ROI) for a brief moment. This effectively reduces the fluorescence in the local area. Unbleached fluorophore then migrates into the photobleached area as a result of diffusion. The ROI is exposed to low intensity fluorescence excitation conditions and snapshots are taken at discrete time steps. The intensity is averaged over the ROI for the recovery time [35]. The characteristic time of diffusion is then calculated from the 50% recovery mark of the normalized data. An illustration of the measured recovery for a FRAP experiment can be seen in Figure

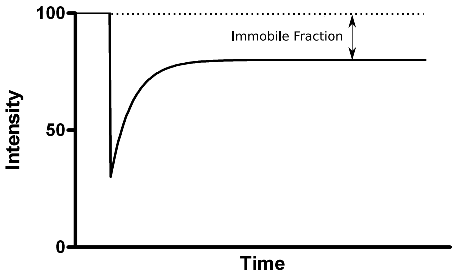

Figure 8.1: Depiction of a measured recovery over the ROI for a typical FRAP experiment. As the recovery continues, the intensity reaches a maximum less than that of the pre-bleach intensity. This is referred to as an immobile fraction.

The diffusivity of the medium can then be calculated. FRAP experiments today are most frequently conducted with a Confocal Scanning Laser Microscope (CSLM). Common fluorophores to study living systems are Green Fluorescent Protein, extrinsic DCI, and fluorescein. Green Fluorescent Protein (GFP) is a widely used to track mobility of membrane bound proteins [70] and proteins found in the inner nuclear membrane of cells [71]. Protein trafficking is easily observed with this technique. Characterizing the mobility of intercellular components and their role in chromatin structure have also been investigated [72]. The well documented use of FRAP has proven it as an effective modality for studying cellular components and processes.

The extensive use of FRAP in biophysical studies to quantitatively calculate diffusivity leaves this method particularly sensitive to inaccuracies. The governing theory assumes ideal fluorophore homogeneity, bleach geometry, and material properties [35]. Along with the theoretical considerations, the physical effects are significant. The physiological effects of high intensity laser bleaching has been linked to phototoxicity [73]. Considering the ideal physical and theoretical conditions, the need for pre-experiment optimization is essential. The high cost in both preparation time and equipment require that the experiment parameters are optimized for each individual material. A simulated experiment allows the user to control both the excitation and material parameters.

FRAP experiments are widely considered the ”gold standard” method of membrane viscosity investigations. Recently, another method has emerged that use molecular rotors. Molecular rotors are fluorescent reporters that exhibit a viscosity dependent quantum yield. FRAP experiments will play an important role in both validating the sensitivity of molecular rotors and comparing the two methods. The primary goal of this paper is to develop and evaluate a FRAP experiment simulation.

The simulation presented is referred to as FrapSim and is modeled after real time FRAP experiments.FrapSim allows the user to model a number of variables including both a single and biexponential recovery. Biexponential recovery behavior commonly arises from the presence of multiple diffusion coefficients. The modeling of biexponential recovery patterns has been reported in diffusion simulations pertaining to water diffusion in neurological tissues [2]. In addition to modeling recovery behavior, variable excitation parameters allow the researcher to simulate a number of physical scenarios.

The output of this simulation is a floating point image stack that can be used to evaluate commercial microscope data analysis software. A main objective of this study is to use the image output of FrapSim to evaluate closed source FRAP software. The majority of data analysis software that accompanies the microscope in question in closed source. This limits the ability of the researcher to compare and contrast the efficacy of the data fitting algorithms to other models. Any black-box systems can be evaluated with test data sets produced in this simulation. The primary objectives of this paper are to evaluate the efficacy of the FrapSim simulation, and to produce an independent data set which can be used to evaluate commercial microscope software.

8.2 Theory

8.2.1 Axelrod Recovery Dynamics

The Axelrod method is the most commonly employed method for recovery of diffusion coefficients. Equation 8.1 is the iterative expression for the fluorescence intensity recovery in a circular region of interest with a Gaussian bleach profile

$$F_k(t) = \frac{qP_0C_0}{A}\sum_{n=0}^{100}[\frac{-K^n}{n!}][1+n(1+\frac{2t}{\tau_D})]^{-1} \tag{8.1}$$

where, q is the combined quantum efficiency of the fluorophore and instrumentation, P_0 is the total laser power, C_0 is the initial fluorophore concentration, A is the laser attenuation factor, $-K$ is the amount of bleaching during time T, τ_D is the "characteristic diffusion time" defined by $\tau_D = w^2/4D$ and t is the time post-bleach. The iterative form describes the normalized fluorescence intensity within the region of interest. Often the fractional form found from experiments is helpful in quickly finding τ_d. The fractional from is computed using Equation 8.2

$$f_k(t) = \frac{F_k(t) - F_k(0)}{F(\infty) - F(0)} \tag{8.2}$$

where $F_k(0)$ is the fluorescence intensity after the photobleach pulse has been applied and $F_(\infty)$ is the maximum intensity level that the ROI reaches after a long recovery period. For a circular beam profile, the fractional form is described as

$$f_k(t) = 1-(\tau_D/t)\exp(-2\tau_D/t)[I_0(2\tau_D/t)+I_2(2\tau_D/t)]+2\sum_{k=0}^{\infty}\frac{(-1)^k(2k+2)!(k+1)!(\tau_D/t)^{k+2}}{(k!)^2[(k+2)!]^2} \tag{8.3}$$

To recover the desired diffusion coefficient, either Equation 8.3 or 8.2 are fit to the recovery data and $\tau_{1/2}$ is found. From here $\tau_{1/2}$ is entered into Equation 8.4. Where w is the half-width at e^{-2} height, and γ_D is a constant dependent on the bleach depth and depth. For a circular beam profile, $\gamma_D = 0.88$ [35].

$$D = \frac{w^2}{4\tau_{1/2}}\gamma_D \tag{8.4}$$

8.2.2 Kapitza Method for Recovery Dynamics

An alternative to the Axelrod method is described by Kapitza. In this method, the bleached fluorophores are quantified and are observed through time with fluorescent images. First a median filter is applied in 3 x 3 neighborhood on the images. Then the first 5 prebleach images are averaged. From here, the post bleach images are subtracted and the bleached fluorophore is plotted on the optical axis. This decay function is shown in Equation **??**.

$$C(0,t) = C_0[1 - \exp(-a^2/4Dt)] + B \tag{8.5}$$

where B is a non-diffusion fraction parameter, D is the diffusion coefficient of the mobile species and C_0 represents the concentration of the diffusible, bleached fluorophore on the optical axis at $t = 0$. The results are then linearized on a semilogarithmic plot and the diffusion coefficient is extracted from the slope of the curve [74]. The efficacy of both fitting methods were compared for the simulated data set.

8.3 Material and Methods

8.3.1 FRAP Experiments

FRAP experiments were conducted on a Leica SP5 CSLM. Poly-l-lactic-acid matrices were soaked in ethanol for 1 hour then rinsed with double distilled water. The matrices were then soaked in a 12 μmol fluorescein (water) solution overnight and then rinsed again with double distilled water. Matrices were cut to size and affixed to Lab-Tek 4 chamber slides with double-sided tape. The chamber was then flooded with Phoshpate Buffered Saline solution. The 10x dry objective was selected for all experiments. The built in FRAP software wizard was then used to perform the bleaching and analysis. An ROI of 70 μm was focused on a homogeneous area in the matrix. The Z-slice was selected so as to maximize the proximity to the topmost layer. The overall laser power, at 488 nm, was set to 30%. The bleaching power was set to 100% and the scanning power was set to 30%. 10 pre-bleach frames were taken along with 10 bleaching frames. The spot was allowed to recover for 100 frames. All frames were 1.314 seconds per slice. The Frap wizard software fit the recovery data with a biexponential association. This suggests the presence of two discrete diffusion coefficients. All microscope generated recovery data was kept and recorded for independent verification.

The image stack from the SP5 was stored in TIFF format for independent image analysis. The secondary analysis was performed using the open source package Crystal Image [75]. The stack of images was first cropped and then converted to grayscale to reduce the size of storage. Next a Greedy Snake [76] implementation was used to isolate the bleached spot. The intensity data of the ROI was then fit to Equations 8.6 and 8.7.

$$y(t) = \mathrm{span}_1 \cdot \exp^{-k_1 \cdot t} \tag{8.6}$$

$$y(t) = \mathrm{span}_1 \cdot \exp^{-k_1 \cdot t} + \mathrm{span}_2 \cdot \exp^{-k_2 \cdot t} \tag{8.7}$$

The equations were implemented in FrapSim using a Levenberg-Marquardt data fitting implementation and independently analyzed using GraphPad Prism 4.0. The fit with the lowest χ^2 was chosen as the best fit. Alternative methods exist for recovering diffusion coefficients from recovery data. The Kapitza is another method that models the recovery of a circular ROI in an exponential fashion. Equations 8.8 and 8.9 were used to fit the data according to the Kapitza method.

$$y(t) = \mathrm{span}_1 \cdot \exp^{\frac{-k_1}{t}} \tag{8.8}$$

$$y(t) = \mathrm{span}_1 \cdot \exp^{\frac{-k_1}{t}} + \mathrm{span}_2 \cdot \exp^{\frac{-k_2}{t}} \tag{8.9}$$

In the Axelrod method, the data is normalized and the time it takes for the fluorescence to recover to 50% of the maximum is noted. Equation 8.10 is used to normalize the recovery data. The result of this normalization gives details about the kinetics of the local fluorophores. If the result of the normalization is less than 100%, there remains a local immobile fraction.

$$MobileFraction = \frac{F(\infty) - F(0)}{F(t < 0) - F(0)} \tag{8.10}$$

Obtaining real world data was an important step in determining suitable starting values for the parameters to be employed.

8.3.2 *Simulation*

The simulation algorithm is based on the classical Laplacian diffusion scheme. All programming was done in C language. The simulation employs an 8 neighbor scheme for increased accuracy. For biexponential diffusion, a scheme was implemented based on previous biexponential recovery. This was done by using a checkerboard pattern in which one of two diffusion coefficients are assigned based on pixel number.

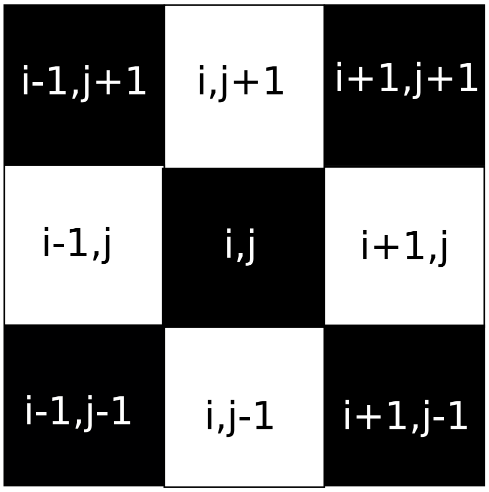

Figure 8.2: The diffusion coefficients are distributed in a checkerboard fashion to produce the desired biexponential diffusion behavior. The black and white squares are assigned different diffusion coefficients. This approach has been used to model water diffusion in neurological tissue pertaining to MRI [2].

To accurately simulate a photobleaching experiment, Gaussian distributions were used for both the laser power and additive noise. The code for the Gaussian noise with random number seeding was based on Numerical Recipes in C [77]. Other important features of the simulation are the ability to control recovery time, bleach time, laser beam radius, noise level, and time per slice. A graphic user interface (GUI) was created, to handle these parameters, using Glade. Glade is an open source frontend for the GTK library [78]. The exponential fits previously described were fit to the recovery data with a Levenberg-Marquardt implementation found in the GNU Scientific Library [79]. Once the simulation was constructed, the ability to simulate real life conditions was evaluated by generating data sets with varying diffusion coefficients. The other parameter values used were based on realistic conditions found from the previously described experiments. Simulated data was generated with the FrapSim software and then analyzed with the programmed Levenberg-Marquardt fits and independently with GraphPad Prism 4.0. The fits and results were then compared.

8.3.3 *SP5 Comparison*

The FrapSim program generates a IEEE float image stack saved in the raw format. The Leica SP5 is configured to analyze "Leica Image Format", abbreviated LIF, image files. LIF files are comprised of a header region that is used to record critical experiment data and settings. A primary objective is to generate a data set with known parameters and compare the fitting capabilities of both native and non-native statistical analysis programs. To achieve this, the simulation data must be compatible with the closed source Leica software and its LIF data format.

The first step in generating data that is accessible to the Leica SP5 is to investigate the proprietary LIF format. The LIF files generated by the Leica software are 8 bit image files accompanied by a XML style header. The XML header contains experiment parameters and description along with path information. To create a LIF file independent of the microscope, an experiment was conducted and saved in the LIF format. The file was then analyzed and found to have a short (130kb) header region. The header was then split from the LIF file and attached to the FrapSim generated raw file. The FrapSim file first had to be converted to 8 bit from IEEE floating point values. The image was then renamed in the LIF format. The custom generated LIF file was immediately able to be accessed through the Leica Frap Wizard analysis program.

8.4 Results and Discussion

8.4.1 FRAP Experiments

The behavior of fluorescein in the PLLA matrices was investigated with FRAP experiments performed on the SP5 microscope. From these experiments, we were able to characterize the diffusion properties on which the model would be based. Figure 8.3 shows the images acquired through the Leica software. Characterizing the diffusive behavior was a vital step in the development of FrapSim.

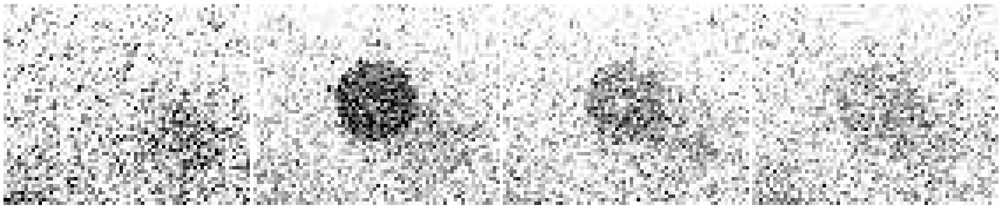

(a) $t = prebleach$ (b) $t = 0$ (c) $t = 70s$ (d) $t = \infty$

Figure 8.3: FRAP experiment for PLLA matrix stained with fluorophore. As Figure 8.3d shows, a faint bleached spot remains suggesting the presence of an immobile fraction.

Analysis with the built-in analysis software suggests the presence of two diffusing species. These results were independently confirmed with the use of GraphPad Prism data fitting software by using the F-test to determine if a single exponential fit would be more appropriate. The Leica SP5 does not allow for this analysis. It is important to note that analysis through residuals only tells half the story of a true fit. The F-test determines if additional model parameters are statistically justified by accounting for the degrees of freedom. This is an essential step for determining the goodness of fit for a particular model.

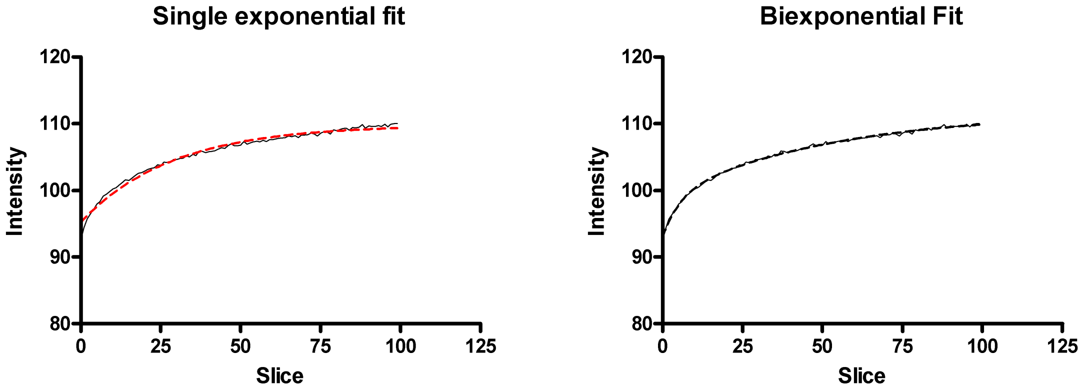

Figure 8.4: The biexponential fit of the experimental data in Figure 8.3 is confirmed through the F-test. This behavior is indicative of multiple diffusing species. The biexponential fit is preferred with $P < 0.001$.

Both the Leica Frap Wizard and the external data analysis suggest a biexponential recovery. This behavior is believed to be an artifact of the porous nature of the material. The high porosity may give rise to areas with discretely different diffusivities. The Frap Wizard had a tendency to incompletely converge towards the final values whereas the GraphPad solver always converged. Although the biexponential recovery was confirmed in both methods, the Frap Wizard had a tendency towards unstable convergence values. The Frap Wizard would continually change the goodness of fit after multiple iterations of data fitting. This is a significant consideration when reporting quantitative diffusion coefficients. This characterization was critical to accurately model the diffusive properties of the PLLA matrices.

8.4.2 *Simulation*

The response of the simulation to single diffusion coefficients was evaluated. Figure 8.5 shows the results of these experiments. The simulated experiment only modeled a single exponential recovery, yet, the diffusivity values suggest both diffusion coefficients are changing with each run. While the difference is low, the trend is still significant. This is an artifact of the fitting algorithm used in the Levenberg-Marquardt implementation. Figure 8.5 displays multiple diffusion coefficients. The results reflect the limitations of the current data fitting methods and the proclivity of these methods to inaccurately model recovery behaviors.

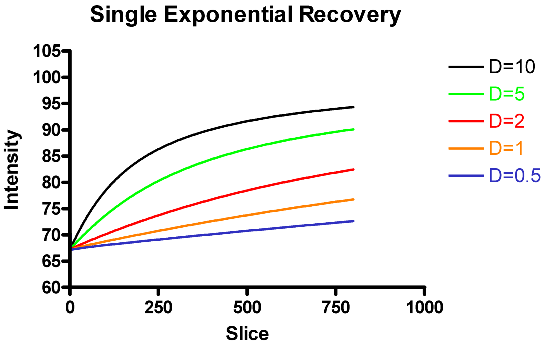

Figure 8.5: The response to changing diffusion coefficients is evaluated. For each run, a single exponential recovery is simulated keeping all other parameters constant.

All data fitting algorithms are subject to error. This error is amplified in the case of multiple diffusing species. The ability to detect minuscule changes in diffusion is hindered in this case. Signal-to-Noise Ratio (SNR) plays a vital role in determining the appropriate fit for the data. FrapSim allows users to use additive noise to simulate this real world effect. The additive noise function is evaluated and shown in Figure 8.6. All diffusion coefficients and other vital parameters were kept constant while only the noise level was altered. The intensity values were modulated for display purposes only.Units of standard deviation were used to evaluate the effects of noise on the experiment.

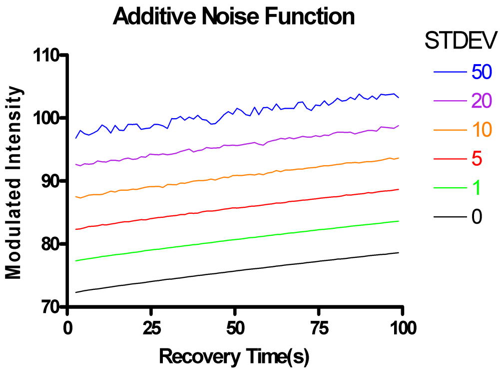

Figure 8.6: The sensitivity to noise is shown above. All parameters were kept constant while the noise level was increased. A diffusion coefficient of 5 was chosen for this experiment. The intensity levels were modulated for viewing purposes only.

The ability to detect small differences between multiple diffusing species is often difficult to achieve. This inability of detection arises from the fitting algorithms used within data analysis programs. The detection of both a weak and strong diffusion coefficient was evaluated. The order of magnitude was altered between two diffusion coefficients to achieve this. One coefficient was kept constant while the other was altered by an order of magnitude. The results are shown in Figure 8.7. The results of this experiment statistically show the presence of two diffusion coefficients. This is as expected and furthermore shows the robustness to detect multiple diffusion coefficients.

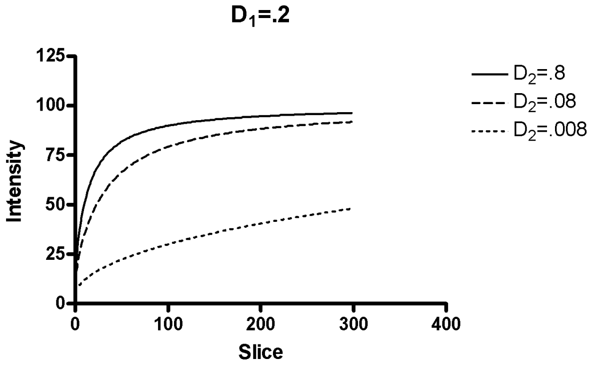

Figure 8.7: Statistical analysis confirms the presence of multiple diffusing species between for all differences in order of magnitude. One diffusion coefficient was held constant with $D_1 = 0.2$, whereas the second diffusion coefficient was varied

8.4.3 *SP5 Validation*

The SP5 analysis software was tested to evaluate changes in diffusion coefficient, noise levels, and immobile fraction. In the first set of experiments a single exponential recovery was simulated. In addition, a biexponential recovery was simulated. The next set simulated the sensitivity to noise by altering the additive noise level. The final set of experiments evaluated the ability of the data analysis methods to detect changes in the immobile fraction.

Table 8.1 shows the results of simulating a single diffusing species. The extracted diffusion coefficients display a linear trend with increasing D_1. The FrapSim and SP5 fits are comparable except from $D = 2$. For FrapSim, the data fitting algorithm does not converge at this value. This behavior was confirmed through a repeat experiment.

Table 8.1: Recovered diffusion coefficients from simulation and SP5 software

$D_1 = D_2$	SP5	FrapSim
0.5	2.16	1.92
1	3.46	3.18
2	6.71	*DNC*
5	14.68	14.44
10	23.96	23.78

The next experiment compared the ability to detect multiple diffusing species. The results are shown in Table 8.2. The SP5 biexponential fit results in identical values for both exponential rates. This is equivalent to a single exponential recovery. The FrapSim coefficients are independently changing suggesting a biexponential recovery. One important point is that the recovered coefficients are not in the same range as the simulated values. Longer recovery times have yielded much better fits. This may be indicative of a dynamic system that results from diffusion occurring during the bleaching process.

Table 8.2: Recovered diffusion coefficients from simulation and SP5 software

Simulated		Sp5		FrapSim	
D_1	D_2	D_1	D_2	D_1	D_2
0.5	1	2.03	2.04	224.6	1.92
0.5	2	2.36	2.37	280.6	2.37
0.5	5	2.69	2.69	334.32	2.73
0.5	10	2.82	2.82	357.45	2.88

Next, the effect of the immobile fraction on the ability to recover the diffusion coefficient was evaluated. As seen in Table 8.3, both recovered diffusion coefficients were consistent and unaffected by the increasing immobile fraction. This is the expected result, as the immobile fraction should not affect the recovery rate of the diffusing species.

Table 8.3: List of extracted diffusion coefficients for $D = 0.5$, with varying levels of immobile fraction. All other parameters were kept constant

Immobile Fraction	SP5	FrapSim
0	14.68	14.44
5	14.68	14.44
10	14.68	14.44
20	14.68	14.44

Finally, additive noise was employed to determine the effects on data fitting. In this experiment set the FrapSim was much more resistant to noise when fitting the recovery behavior. Table 8.4 shows the results of the noise experiments.

Table 8.4: List of extracted diffusion coefficients, for a simulated $D = 0.5$, with varying levels of additive noise. All other parameters were kept constant

Noise Level (STDEV)	SP5	FrapSim
0	14.68	14.44
1	14.68	14.44
5	14.57	14.44
10	14.64	14.44
20	14.74	14.59
50	13.65	14.44

The experiments for the SP5 comparison give insight into the robustness of our open source data fitting algorithm. The exceptional noise resistance is a key feature of the open source data fitting algorithm. The ability to evaluate these closed source algorithms not only evaluates the system in question, but gives researchers a chance to compare methods for the optimal implementation.

8.5 CONCLUSION

We have successfully demonstrated a simulation that is useful for both experiment optimization and closed source software evaluation. Developing a simulation catered to actual experiment conditions is necessary. FrapSim has been developed with all the necessary parameters needed to simulate a real time experiment. The numerical stability of this model suggests an accurate depiction of the diffusion process. The ability to simulate FRAP experiments is vital for optimization of membrane diffusivity studies. The simulation showed particular robustness to the detection of multiple diffusing species and changes in beam profile. Continuing to improve the accuracy of recovered coefficients will be the next step in the development. Combining the results from FrapSim along with the FRAP experiments have given us great insight into the limitations and dynamics of the bleaching and recovery processes. Open source access allows for the utmost transparency and understanding of the recovery dynamics and the equations used to fit them.

Chapter 9

Research Conclusion

The central theme of this research has been the investigations of biomembranes with fluorescence based methods. The use of ratiometric rotors in biomembrane systems is the next iteration after the initial publication of intensity based measurements with molecular rotors. We have evaluated a group of ratiometric molecular rotors and characterized the viscosity sensitivity and spectral response. The successful incorporation of these dyes into phospholipid membrane systems is a significant forward step towards cellular integration. The excellent temporal and spatial resolution in response to marginal changes in apparent membrane viscosity is an important attribute that may prove valuable to researchers and clinicians alike. Fluorescence based methods are privy to a host of obstacles and considerations in the pursuit of accurate measurements. The fluroviscometer is our attempt to account for these.

Commercial spectrophotometers are accurate instruments for detecting and quantifying fluorescence signals in clear, non-absorbing, non-scattering samples. Unfortunately, fluorescence samples sometimes exhibit non-ideal optical properties that skew fluorescence measurements. A solution with high amounts of phospholipid, such as our liposomes, is a classic example of a turbid media. This is of great importance for intensity based measurements. Commercial spectrophotometers lack the necessary instrumentation for correcting these effects. We have built a fluorophotometer capable of measuring fluorescence spectra and the absorbance of the sample. Additionally, we have implemented a system with a non-exciting laser that allows us to quantify the sample turbidity. The successful demonstration and comparison with commercial equipment is an important and necessary step towards the instrument optimization with molecular rotors. Molecular rotors are an emerging method for characterizing membrane viscosity. The gold standard in use today is fluorescence recovery after photobleaching (FRAP).

Demonstrating the efficacy of molecular rotors compared to FRAP experiments is a future goal of this research. FRAP experiments exhibit a high cost of entry in both equipment and time. Pre-experiment optimization is an important step to obtaining reliable experiment results in the least time. We have constructed and evaluated a simulation with multiple controllable parameters. Furthermore, we have evaluated the closed source data fitting software with our open source simulation data. The open source aspect of this research encourages examination of the inner workings of data fitting and optimization.

Molecular rotors are exciting new tools that have shown promise for viscosity measurement with the cellular membrane. Advances in instrumentation and simulation will play a central role in driving this research. The further synthesis of ratiometric dyes will bring improvements in membrane incorporation. This is the first step towards cellular integration. Combining all of these approaches will further the development of molecular rotors as tool for biophysical research.

BIBLIOGRAPHY

[1] MA. Haidekker, ME. Nipper, A. Mustafic, D. Lichlyter, M. Dakanali, and EA Theodorakis. *Advanced Fluorescence Reporters in Chemistry and Biology I. Fundamentals and Molecular Design.*, volume 8 of *Springer Series on Fluorescence*. Springer-Verlag, 2010.

[2] Chih-Liang Chin, Felix W. Wehrli, Scott N. Hwang, Masaya Takahashi, and David B. Hackney. Biexponential diffusion attenuation in the rat spinal cord: computer simulations based on anatomic images of axonal architecture. *Magn Reson Med*, 47(3):455–460, Mar 2002.

[3] J. R. Lakowicz. *Principles of Fluorescence Spectroscopy.* Kluwer Academic/Plenum Publishers, New York, 1999.

[4] E. Lippert, W. Luder, and H. Boos. Advances in molecular spectroscopy, ed. by a. *Mangini (Pergamon, Oxford 1962) p*, 443.

[5] K. Rotkiewicz, K. H. Grellmann, and Z. R. Grabowski. Reinterpretation of the anomalous fluorescense of pn, n-dimethylamino-benzonitrile. *Chemical Physics Letters*, 19(3):315–318, 1973.

[6] W. Rettig and R. Lapouyade. Fluorescence probes based on twisted intramolecular charge transfer (tict) states and other adiabatic photoreactions. *Topics in fluorescence spectroscopy*, pages 109–149, 2002.

[7] Z. R. Grabowski and J. Dobkowski. Twisted intramolecular charge transfer (tict) excited states: energy and molecular structure. *Pure Appl. Chem*, 55:245, 1983.

[8] C. Rullière, Z. R. Grabowski, and J. Dobkowski. Picosecond absorption spectra of carbonyl derivatives of dimethylaniline: the nature of the tict excited states. *Chemical Physics Letters*, 137(5):408–413, 1987.

[9] K. A. Zachariasse, M. Grobys, T. von der Haar, A. Hebecker, Y. V. Il'ichev, Y. B. Jiang, O. Morawski, and W. Kühnle. Intramolecular charge transfer in the excited state. kinetics and configurational changes. *Journal of Photochemistry and Photobiology A: Chemistry*, 102(1):59–70, 1996.

[10] Y. V. Il'ichev, W. Kuhnle, and K. A. Zachariasse. Intramolecular charge transfer in dual fluorescent 4-(dialkylamino) benzonitriles. reaction efficiency enhancement by increasing the size of the amino and benzonitrile subunits by alkyl substituents. *J. Phys. Chem. A*, 102(28):5670–5680, 1998.

[11] O. Kajimoto, M. Futakami, T. Kobayashi, and K. Yamasaki. Charge-transfer-state formation in supercritical fluid:(n, n-dimethylamino) benzonitrile in trifluoromethane. *The Journal of Physical Chemistry*, 92(5):1347–1352, 1988.

[12] L. A. Diverdi and M. R. Topp. Subnanosecond time-resolved fluorescence of acridine in solution. *The Journal of Physical Chemistry*, 88(16):3447–3451, 1984.

[13] M. A. El-Sayed and M. Kasha. Interchange of orbital excitation types of the lowest electronic states of 2 ring n−heterocyclics by solvation. 1959.

[14] G. G. Guilbault. *Practical fluorescence*. CRC, 1990.

[15] T. Förster and G. Hoffmann. Die viskositätsabhängigkeit der fluoreszenzquantenausbeuten einiger farbstoffsysteme. *Z. Phys. Chem.(Munich)*, 75:63–76, 1971.

[16] M. A. Haidekker and E. A. Theodorakis. Environment-sensitive behavior of fluorescent molecular rotors – a review. *Journal of Biological Engineering (submitted)*, 2010.

[17] T. Gustavsson, L. Cassara, S. Marguet, G. Gurzadyan, P. Meulen, S. Pommeret, and J. C. Mialocq. Rotational diffusion of the 7-diethylamino-4-methylcoumarin c1 dye molecule in polar protic and aprotic solvents. *Photochemical & Photobiological Sciences*, 2(3):329–341, 2003.

[18] T. Iio, S. Takahashi, and S. Sawada. Fluorescent molecular rotor binding to actin. *Journal of biochemistry*, 113(2):196, 1993.

[19] R. O. Loutfy and B. A. Arnold. Effect of viscosity and temperature on torsional relaxation of molecular rotors. *The Journal of Physical Chemistry*, 86(21):4205–4211, 1982.

[20] A. Gierer and K. Wirtz. Molecular theory of microfriction. *Z Naturforsch*, 8:532–538, 1953.

[21] M. Vogel and W. Rettig. Excited state dynamics of triphenylmethane-dyes used for investigation of microviscosity effects. *Berichte der Bunsengesellschaft für Physikalische Chemie*, 91(11):1241–1247, 1987.

[22] A. K. Doolittle. Studies in newtonian flow. iii. the dependence of the viscosity of liquids on molecular weight and free space (in homologous series). *Journal of Applied Physics*, 23:236, 1952.

[23] R. O. Loutfy. Fluorescence probes for polymer free-volume. *NATO ASI series. Series C, Mathematical and physical sciences*, 182:429–448, 1986.

[24] F. M. White. *Fluid Mechanics.* McGraw Hill, 1999.

[25] M. Shinitzky. *Physiology of membrane fluidity.* CRC, 1984.

[26] S. J. Singer and G. L. Nicolson. The fluid mosaic model of the structure of cell membranes. *Science*, 175(23):720–731, 1972.

[27] D. Zakim, J. Kavecansky, and S. Scarlata. Are membrane enzymes regulated by the viscosity of the membrane environment. *Biochemistry*, 31(46):11589–11594, 1992.

[28] M. M. Gleason, M. S. Medow, and T. N. Tulenko. Excess membrane cholesterol alters calcium movements, cytosolic calcium levels, and membrane fluidity in arterial smooth muscle cells. *Circulation research*, 69(1):216, 1991.

[29] O. Nadiv, M. Shinitzky, H. Manu, D. Hecht, C. T. Roberts Jr, D. LeRoith, and Y. Zick. Elevated protein tyrosine phosphatase activity and increased membrane viscosity are associated with impaired activation of the insulin receptor kinase in old rats. *Biochemical Journal*, 298(Pt 2):443, 1994.

[30] W. Osterode, C. Holler, and F. Ulberth. Nutritional antioxidants, red cell membrane fluidity and blood viscosity in type 1 (insulin dependent) diabetes mellitus. *Diabetic Medicine*, 13(12):1044–1050, 1996.

[31] G. S. Zubenko, U. Kopp, T. Seto, and L. L. Firestone. Platelet membrane fluidity individuals at risk for alzheimers disease: a comparison of results from fluorescence spectroscopy and electron spin resonance spectroscopy. *Psychopharmacology*, 145(2):175–180, 1999.

[32] K. Shiraishi, S. Matsuzaki, H. Ishida, H. Nakazawa, and A. Takada. Impaired erythrocyte deformability and membrane fluidity in alcoholic liver disease: participation in disturbed hepatic microcirculation. *Alcohol and Alcoholism. 1993.*, 1993.

[33] Wenxiao Pan, Erik Petersen, Ning Cai, Gang Ma, Jian Run Lee, Zhiqin Feng, Kin Liao, and Kam Leong. Viscoelastic properties of human mesenchymal stem cells. *Conf Proc IEEE Eng Med Biol Soc*, 5:4854–4857, 2005.

[34] R. Lipowsky and E. Sackmann. *Structure and dynamics of membranes.* Elsevier, 1995.

[35] D. Axelrod, D. E. Koppel, J. Schlessinger, E. Elson, and W. W. Webb. Mobility measurement by analysis of fluorescence photobleaching recovery kinetics. *Biophysical journal*, 16(9):1055–1069, 1976.

[36] C. Dietrich, L. A. Bagatolli, Z. N. Volovyk, N. L. Thompson, M. Levi, K. Jacobson, and E. Gratton. Lipid rafts reconstituted in model membranes. *Biophysical Journal*, 80(3):1417–1428, 2001.

[37] D. L. Stenoien, K. Patel, M. G. Mancini, M. Dutertre, C. L. Smith, B. W. O'Malley, and M. A. Mancini. Frap reveals that mobility of oestrogen receptor- is ligand-and proteasome-dependent. *Nature Cell Biology*, 3(1):15–23, 2000.

[38] T. Misteli. Protein dynamics: implications for nuclear architecture and gene expression. *Science*, 291(5505):843, 2001.

[39] J. Davoust, P. F. Devaux, and L. Leger. Fringe pattern photobleaching, a new method for the measurement of transport coefficients of biological macromolecules. *The EMBO Journal*, 1(10):1233, 1982.

[40] K. Braeckmans, L. Peeters, N. N. Sanders, S. C. De Smedt, and J. Demeester. Three-dimensional fluorescence recovery after photobleaching with the confocal scanning laser microscope. *Biophysical Journal*, 85(4):2240–2252, 2003.

[41] M. J. Saxton and K. Jacobson. Single-particle tracking: applications to membrane dynamics. *Annual review of biophysics and biomolecular structure*, 26(1):373–399, 1997.

[42] N. Malchus and M. Weiss. Elucidating anomalous protein diffusion in living cells with fluorescence correlation spectroscopyfacts and pitfalls. *Journal of fluorescence*, 20(1):19–26, 2010.

[43] Gamal Rayan, Jean-Erik Guet, Nicolas Taulier, Frederic Pincet, and Wladimir Urbach. Recent applications of fluorescence recovery after photobleaching (frap) to membrane bio-macromolecules. *Sensors*, 10(6):5927–5948, 2010.

[44] H. M. Munnelly, D. A. Roess, W. F. Wade, and B. G. Barisas. Interferometric fringe fluorescence photobleaching recovery interrogates entire cell surfaces. *Biophysical journal*, 75(2):1131–1138, 1998.

[45] M. E. Nipper, S. Majd, M. Mayer, J. C. M. Lee, E. A. Theodorakis, and M. A. Haidekker. Characterization of changes in the viscosity of lipid membranes with the molecular rotor fcvj. *Biochimica et Biophysica Acta (BBA)-Biomembranes*, 1778(4):1148–1153, 2008.

[46] R. Humphry-Baker, M. Graetzel, and R. Steiger. Drastic fluorescence enhancement and photochemical stabilization of cyanine dyes through micellar systems. *Journal of the American Chemical Society*, 102(2):847–848, 1980.

[47] C. E. Kung and J. K. Reed. Microviscosity measurements of phospholipid bilayers using fluorescent dyes that undergo torsional relaxation. *Biochemistry*, 25(20):6114–6121, 1986.

[48] S. Lukac. Thermally induced variations in polarity and microviscosity of phospholipid and surfactant vesicles monitored with a probe forming an intramolecular charge-transfer complex. *Journal of the American Chemical Society*, 106(16):4386–4392, 1984.

[49] M. L. Viriota, M. C. Carréa, C. Geoffroy-Chapotota, A. Brembillab, S. Mullerc, and J. F. Stoltzc. Molecular rotors as fluorescent probes for biological studies. *Clinical Hemorheology and Microcirculation*, 19(2):151–160, 1998.

[50] P. F. Davies. Flow-mediated endothelial mechanotransduction. *Physiological reviews*, 75(3):519, 1995.

[51] M. A. Haidekker, N. L'Heureux, and J. A. Frangos. Fluid shear stress increases membrane fluidity in endothelial cells: a study with dcvj fluorescence. *American Journal of Physiology- Heart and Circulatory Physiology*, 278(4):H1401, 2000.

[52] M. A. Haidekker, T. Ling, M. Anglo, H. Y. Stevens, J. A. Frangos, and E. A. Theodorakis. New fluorescent probes for the measurement of cell membrane viscosity. *Chemistry & biology*, 8(2):123–131, 2001.

[53] E. A. Haigh, K. R. Thulborn, L. W. Nichol, and W. H. Sawyer. Uptake of n-(9-anthroyloxy) fatty acid fluorescent probes into lipid bilayers. *Australian journal of biological sciences*, 31(5):447, 1978.

[54] K. R. Thulborn and W. H. Sawyer. Properties and the locations of a set of fluorescent probes sensitive to the fluidity gradient of the lipid bilayer. *Biochimica et Biophysica Acta (BBA)-Biomembranes*, 511(2):125–140, 1978.

[55] M. Angelova, S. Soleau, P. Meleard, F. Faucon, and P. Bothorel. Preparation of giant vesicles by external ac electric fields. kinetics and applications. *Trends in Colloid and Interface Science VI*, pages 127–131, 1992.

[56] H. V. Ly and M. L. Longo. The influence of short-chain alcohols on interfacial tension, mechanical properties, area/molecule, and permeability of fluid lipid bilayers. *Biophysical journal*, 87(2):1013–1033, 2004.

[57] J. Traube. Ueber die capillaritätsconstanten organischer stoffe in wässerigen lösungen. *Justus Liebigs Annalen der Chemie*, 265(1):27–55, 1891.

[58] P. Yeagle and P. L. Yeagle. *The membranes of cells.* Academic Press San Diego, CA, 1993.

[59] H. Ferreira, M. Lúcio, B. de Castro, P. Gameiro, J. L. F. C. Lima, and S. Reis. Partition and location of nimesulide in epc liposomes: a spectrophotometric and fluorescence study. *Analytical and bioanalytical chemistry*, 377(2):293–298, 2003.

[60] M. Lúcio, H. Ferreira, J. L. F. C. Lima, C. Matos, B. Castro, and S. Reis. Influence of some anti-inflammatory drugs in membrane fluidity studied by fluorescence anisotropy measurements. *Physical Chemistry Chemical Physics*, 6(7):1493–1498, 2004.

[61] P. Nair, S. Singh Kanwar, and S. Nath Sanyal. Effects of non steroidal anti-inflammatory drugs on the antioxidant defense system and the membrane functions in the rat intestine. *Nutrición Hospitalaria*, 21:638–649, 2006.

[62] S. Majd and M. Mayer. Hydrogel stamping of arrays of supported lipid bilayers with various lipid compositions for the screening of drug-membrane and protein-membrane interactions. *Angewandte Chemie*, 117(41):6855–6858, 2005.

[63] D. M. Soumpasis. Theoretical analysis of fluorescence photobleaching recovery experiments. *Biophysical journal*, 41(1):95–97, 1983.

[64] M. A. Haidekker, T. P. Brady, D. Lichlyter, and E. A. Theodorakis. A ratiometric fluorescent viscosity sensor. *J. Am. Chem. Soc*, 128(2):398–399, 2006.

[65] M. O. Eze. Membrane fluidity, reactive oxygen species, and cell-mediated immunity: implications in nutrition and disease. *Medical hypotheses*, 37(4):220–224, 1992.

[66] D. S. Heron, M. Shinitzky, M. Hershkowitz, and D. Samuel. Lipid fluidity markedly modulates the binding of serotonin to mouse brain membranes. *Proceedings of the National Academy of Sciences of the United States of America*, 77(12):7463, 1980.

[67] T. Koike, G. Ishida, M. Taniguchi, K. Higaki, Y. Ayaki, M. Saito, Y. Sakakihara, M. Iwamori, and K. Ohno. Decreased membrane fluidity and unsaturated fatty acids in niemann-pick disease type c fibroblasts. *Biochimica et Biophysica Acta (BBA)-Molecular Basis of Disease*, 1406(3):327–335, 1998.

[68] D. Fischer, E. A. Theodorakis, and M. A. Haidekker. Synthesis and use of an in-solution ratiometric fluorescent viscosity sensor. *Nature Protocols*, 2(1):227–236, 2007.

[69] M. I. Angelova and D. S. Dimitrov. Liposome electroformation. *Faraday Discussions of the Chemical Society*, 81:303–311, 1986.

[70] C. Favard, N. Olivi-Tran, and J. L. Meunier. Membrane bound protein diffusion viewed by fluorescence recovery after bleaching experiments : models analysis. 2002.

[71] J. Ellenberg, E. D. Siggia, J. E. Moreira, C. L. Smith, J. F. Presley, H. J. Worman, and J. Lippincott-Schwartz. Nuclear membrane dynamics and reassembly in living cells:

targeting of an inner nuclear membrane protein in interphase and mitosis. *J Cell Biol*, 138(6):1193–1206, Sep 1997.

[72] Martin E. van Royen, Pascal Farla, Karin A. Mattern, Bart Geverts, Jan Trapman, and Adriaan B. Houtsmuller. Fluorescence recovery after photobleaching (frap) to study nuclear protein dynamics in living cells. *Methods Mol Biol*, 464:363–385, 2009.

[73] Y. Chen, B. C. Lagerholm, B. Yang, and K. Jacobson. Methods to measure the lateral diffusion of membrane lipids and proteins. *Methods*, 39(2):147–153, 2006.

[74] H. G. Kapitza, G. McGregor, and K. A. Jacobson. Direct measurement of lateral transport in membranes by using time-resolved spatial photometry. *Proc Natl Acad Sci U S A*, 82(12):4122–4126, Jun 1985.

[75] M. A. Haidekker. *Advanced Biomedical Image Analysis (In Press)*. Wiley, 2010.

[76] D. J. Williams and M. Shah. A fast algorithm for active contours and curvature estimation. *CVGIP: Image understanding*, 55(1):14–26, 1992.

[77] H. William, S. A. Teukolsky, W. T. Vetterling, and B. P. Flannery. *Numerical Recipes in C: The art of scientific computing*. Cambridge university press New York, NY, USA, 1988.

[78] The gtk+ project, http://www.gtk.org/, 2010.

[79] B. Gough. Gnu scientific library reference manual. 2009.